

1 Evolution of Cloud Droplet Temperature and Lifetime in 2 Spatiotemporally Varying Subsaturated Environments with 3 Implications for Ice Nucleation at Cloud Edges 4

5 Puja Roy^{1,2}, Robert M. Rauber¹, Larry Di Girolamo¹

6 ¹[Department of Climate, Meteorology & Atmospheric Sciences, University of Illinois Urbana-Champaign, USA](#)

7 ²[Research Applications Laboratory, NSF National Center for Atmospheric Research, USA](#)

8
9
10 *Correspondence to:* Puja Roy (pujaroy@ucar.edu)

11
12 **Abstract.** Ice formation mechanisms in generating cells near stratiform cloud-tops, where mixing and entrainment
13 occurs in the presence of supercooled water droplets, remain poorly understood. Supercooled cloud droplet
14 temperature and lifetime may impact heterogeneous ice nucleation through contact and immersion freezing; however,
15 modeling studies normally assume droplet temperature to be spatially uniform and equal to the ambient temperature.
16 Here, we present a first-of-its-kind quantitative investigation of the temperature and lifetime of evaporating droplets,
17 considering internal thermal gradients within the droplet as well as thermal and vapor density gradients in the
18 surrounding air. Our approach employs solving the Navier-Stokes and continuity equations, coupled with heat and
19 vapor transport, using an advanced numerical model. For typical ranges of cloud droplet sizes and environmental
20 conditions, the droplet internal thermal gradients dissipate quickly (≤ 0.3 s) when droplets are introduced to new
21 subsaturated environments. However, the magnitude of droplet cooling is much greater than estimated from past
22 studies of droplet evaporation, especially for drier environments. For example, for an environment with pressure of
23 500 hPa, and ambient temperature far from the droplet of -5°C , the droplet temperature reduction can be as high as
24 24, 11, and 5°C for initial ambient relative humidities of 10%, 40%, and 70% respectively. Droplet lifetimes are found
25 to be tens of seconds longer compared to previous estimates due to weaker evaporation rates because of lower droplet
26 surface temperatures. Using these new end-of-lifetime droplet temperatures, the enhancement in activation of ice-
27 nucleating particles predicted by current ice nucleation parameterization schemes is discussed.

Deleted: ²

Deleted: ²

Moved down [8]: ¹Research Applications Laboratory, NSF
National Center for Atmospheric Research¹

Deleted: ²

Moved (insertion) [8]

Deleted: ¹

36 **1 Introduction**

37
38 Ice formation often occurs near cloud tops of stratiform clouds where ice-generating cells (AMS 2024) are frequently
39 found in a variety of cold, cloudy environments (Plummer et al., 2014; Ramelli et al., 2021). These cells play a crucial
40 role in primary ice nucleation and growth (Tessendorf et al., 2015). Evidence of mixing and entrainment and the
41 presence of supercooled liquid water within and between the highly turbulent cells has been observed (Plummer et al.,
42 2014; Wang et al., 2020; Zaremba et al., 2024). Within regions of entrainment and mixing at cloud boundaries, cloud
43 droplets are exposed to subsaturated environments and undergo evaporation that leads to droplet temperatures that
44 could be several degrees lower than that of the ambient environment (Kinzer and Gunn, 1951; Watts, 1971; Roy et
45 al., 2023). However, in modeling cloud microphysical processes, the difference in temperature between the cloud
46 droplets and their environment is generally assumed to be negligible (Pruppacher and Klett, 1997), i.e., the droplets'
47 temperatures are approximated to be the same as that of their ambient environment. This assumption is reasonable for
48 cloud droplets inside the cloud but breaks down within entrainment and mixing zones at cloud boundaries and may
49 lead to uncertainties in the numerical simulations of microphysical processes. Cloud droplet temperatures affect the
50 calculated droplet diffusional growth or evaporation rates (Roach 1976; Srivastava and Coen 1992; Marquis and
51 Harrington 2005; Roy et al., 2023), and droplet lifetimes (Roy et al., 2023), radiative effects via temperature-dependent
52 refractive indices (Rowe et al. 2020), and ice formation via pathways that require supercooled liquid water droplets,
53 such as contact nucleation (Young, 1974), immersion freezing (Szakáll et al., 2021), and homogeneous nucleation
54 (Khvorostyanov and Sassen, 1998; Khain and Pinsky, 2018). These uncertainties can propagate into microphysical
55 parameterization schemes, leading to possible inadequate representation of mixed-phase cloud properties across
56 various scales (e.g., Large Eddy Simulations (LES), Cloud Resolving Models (CRM), Climate Models), impacting
57 predictions of precipitation or climate change.

58
59 Several studies have highlighted the special importance of the air-water interface of the water droplet during ice
60 nucleation. Many experimental and theoretical studies have suggested that ice initiation occurs at the droplet surface
61 (Tabazadeh et al., 2002a; Tabazadeh et al., 2002b; Djikaev et al., 2002; Satoh et al. 2002; Shaw et al., 2005) and the
62 interface thermodynamically favors the contact mode over the immersion freezing mode (Djikaev and Ruckenstein,
63 2008). Based on their laboratory observations, Tabazadeh et al., (2002a) suggested that homogeneous nucleation of
64 nitric acid dihydrate (NAD) and nitric acid trihydrate (NAT) particles within aqueous nitric acid droplets primarily
65 occurs at the droplet surface. This leads to the hypothesis that phase transformations in atmospheric aerosols may
66 predominantly be surface-based (Tabazadeh et al., 2002b), challenging the traditional theory of homogeneous
67 crystallization where freezing begins inside the volume of the droplet (Volmer, 1939). Satoh et al. (2002) studied
68 cooling and freezing in water droplets due to evaporation in an evacuated chamber and found that droplets rapidly
69 froze with significant supercooling, with the freezing initiated from the droplet surface. Studies employing molecular
70 dynamics simulations (Chushak et al., 1999, 2000) and thermodynamic calculations (Djikaev et al., 2002) additionally
71 corroborate that a crystalline nucleus preferentially forms at the droplet surface rather than within the bulk droplet
72 volume. Laboratory observations from Shaw et al., (2005) reveal that freezing temperatures are 4-5 K higher when an

73 ice-forming nucleus is closer to the surface of a supercooled water droplet compared to when it's immersed within the
74 droplet. They found that the nucleation rate at the water surface is significantly higher (by a factor of 10^{10}) than in the
75 bulk droplet, indicating that the free energy required for critical ice germ formation decreases when near the air-water
76 interface, and the jump frequency of molecules from the liquid to the solid phase may be significantly enhanced at the
77 interface. Lü et al., (2005) conducted ice nucleation experiments with acoustically levitated supercooled water
78 droplets. ~~Using statistical analyses of nucleation rates, they found that~~ ice nucleation predominantly initiates in the
79 vicinity of the droplet surface. Therefore, given the importance of the droplet surface in ice nucleation and since
80 evaporation is a surface phenomenon, in the quest to better understand the physical mechanisms responsible for
81 primary ice nucleation, it is important to accurately investigate the thermal evolution of the evaporating droplet surface
82 as well as the internal thermal gradients within the supercooled droplet, as ice nucleation is highly temperature
83 dependent.

84
85 Few studies in the cloud microphysics literature have carried out explicit numerical estimations and evolutions of
86 supercooled, evaporating cloud droplet temperatures and lifetimes for a wide range of environmental conditions. Roy
87 et al., (2023) provides a comprehensive review of past theoretical, numerical, or experimental studies of droplet
88 evaporation. Most of these studies examined the evaporation of raindrops for above ~~0°C~~ temperatures (Kinzer and
89 Gunn, 1951; Watts 1971; Watts and Farhi, 1975), either assuming steady-state expressions (Beard and Pruppacher,
90 1971) or simplifying assumptions of linear dependence of saturation vapor density on temperature (Kinzer and Gunn,
91 1951; Watts 1971; Watts and Farhi, 1975). Srivastava and Coen (1992) assumed the heat storage term in the droplet
92 heat budget to be negligible, and investigated the evaporation of isolated, stationary hydrometeors by iteratively
93 solving the steady-state solutions, using saturation vapor pressure relations from Wexler (1976) to calculate the
94 saturation vapor density. Roy et al., (2023), by including the heat storage term and solving for time-dependent heat
95 and mass transfer between single, stationary cloud droplets evaporating in infinitely large, prescribed ambient
96 environments, demonstrated that the temperatures of the cloud droplets (initial radii between 30-50 μm) reach steady-
97 state quite quickly (within <0.5 s). They considered a wide range of environmental conditions and found that
98 evaporating droplet temperatures can typically be 1-5 K colder than that of the environment, with values as low as
99 ~ 10 K for low relative humidity, and low-pressure conditions ~~with~~ near 0°C environments. Their steady-state droplet
100 temperatures agreed well with those of Srivastava and Coen (1992). They showed that the droplet temperature during
101 evaporation can be approximated by the thermodynamic wet-bulb temperature of the ambient environment. For most
102 subsaturated conditions, radiative cooling in cloud-top environments was found to play a negligible role in altering
103 evaporating droplet temperatures, except for larger droplets in environments close to saturation.

104
105 However, two main issues have not yet been accounted for in the aforementioned studies. Firstly, water droplets were
106 considered to have a uniform bulk droplet temperature, based on the assumption of infinite thermal heat conductivity
107 of water, thus ignoring the added complexity of simulating the internal thermal gradients within the droplet. (Kinzer
108 and Gunn, 1951; Watts, 1971; Srivastava and Coen, 1992, Roy et al., 2023). As several studies suggest that the droplet
109 surface plays a special role in nucleating ice and evaporation being a surface phenomenon, accurate modeling of the

Deleted: and

Deleted: that statistical analyses of nucleation rates indicate

Deleted: zero

113 evolution of droplet surface temperature and internal thermal gradients within the droplet volume is required to
114 correctly predict the ice nucleation rates. Secondly, to date, none of these studies considered the spatiotemporally
115 evolving effects of thermal and moisture feedback between the droplet and its immediate environment. The rationale
116 for justifying the usage of constant ambient conditions far away from the droplet was mostly based on studies where
117 ambient conditions were defined by prescribed temperature and moisture fields far away from a droplet (Sedunov,
118 1974; Eq. 7.7 of Rogers and Yau, 1989; Srivastava and Coen, 1992). A correction to the ambient conditions at a radius
119 similar to the mean distance between droplets (~1 mm) was shown to lead to minimal modifications for typical cloud
120 conditions (Fukuta, 1992). Thus, this assumption holds for droplets distributed homogeneously in space. Concerning
121 numerically simulating the growth and decay of a droplet population, Grabowski and Yang (2013) stated: “Cloud
122 droplets grow or evaporate because of the presence of moisture and temperature gradients in their immediate vicinity,
123 and these gradients are responsible for the molecular transport of moisture and energy between the droplet and its
124 immediate environment. One may argue that these gradients need to be resolved to represent the growth accurately.
125 Elementary considerations demonstrate that the moisture and temperature gradients in the droplet vicinity are
126 established rapidly [i.e., with a characteristic timescale of milliseconds or smaller (e.g., Vaillancourt et al. 2001, and
127 references therein)]; thus, the steady-state droplet growth equation is accurate enough. More importantly, the volume
128 affected by these gradients has a radius of approximately 10 to 20 droplet radii.... One can simply neglect molecular
129 transport processes in the immediate droplet vicinity and simulate droplet growth using the Maxwellian approach, that
130 is, by applying the supersaturation predicted by the mean (over the volume occupied by the droplet) temperature and
131 moisture fields...(see Vaillancourt et al. 2001, appendix).”

Deleted: classical

132
133 Here, we quantitatively revisit these arguments within the context of an evaporating supercooled cloud droplet. We
134 use high-resolution modeling to resolve the spatiotemporally evolving thermal and vapor density gradients in the
135 vicinity of the droplet as well as include internal heat transfer within the droplet, relaxing the assumption of infinite
136 thermal heat conductivity of water. Using an advanced numerical model, our framework employs the finite-element
137 method to solve the Navier-Stokes and continuity equations, coupled with heat and vapor diffusion, with appropriate
138 boundary conditions. The results from this study extend the findings from Roy et al. (2023) that an evaporating droplet
139 can exist at a temperature lower than that of the ambient environment, and that the temperature deviation increases
140 from the steady-state value under certain environmental conditions. This may lead to significant enhancement in ice
141 nucleation by increasing the predicted number concentrations of activated ice-nucleating particles (INPs) either
142 immersed within or externally contacting the supercooled droplet. The current study advances the numerical approach
143 presented in Roy et al. (2023) by including the impact of internal heat gradients within the droplet and spatiotemporally
144 varying heat and mass transfer between the droplet and its immediate environment. We also provide droplet lifetime
145 comparisons with estimates from Roy et al. (2023) and pure diffusion-limited evaporation calculations. The
146 implications of the evaporating supercooled cloud droplet temperatures and lifetimes on ice nucleation at cloud
147 boundaries are discussed.

148

150 **2 Numerical Methodology**

151 **2.1 Description of COMSOL**

152
153 The simulation of the spatiotemporally varying droplet temperature and radius of an evaporating cloud droplet
154 embedded in a gaseous domain is difficult to solve analytically because of the moving and shrinking boundary at the
155 surface of the evaporating droplet. These kinds of moving boundary problems are known as Stefan problems. To
156 model this process, we have used an advanced numerical solver, COMSOL (Version 6.0), which employs a finite
157 element method to solve partial differential equations (PDEs). The COMSOL Multiphysics software simultaneously
158 uses spatial, material, and mesh coordinate systems described as the spatial frame, material frame, and mesh frame,
159 respectively. The spatial frame is a fixed, global, Euclidean coordinate system, which in 2D has spatial cartesian
160 coordinates (r, z) with the center of the droplet at $(r, z) = (0,0)$ (Fig. 1). The material frame specifies the material
161 substance, in this case, water or air. The mesh frame is a coordinate system used internally by the finite element
162 method.

163
164 The Navier-Stokes and Fick's second law of diffusion equation, which follows from the continuity equation, along
165 with appropriate boundary conditions (see Sec. 3) are solved to conserve mass and momentum in the whole system.
166 The following physics interfaces in COMSOL were used to simulate droplet evaporation: (1) *Two-Phase Laminar*
167 *Fluid Flow*, which includes a moving mesh to track the shrinking water-air interface of the evaporating water droplet
168 and fluid-fluid interface that incorporates evaporative mass flux; (2) *Transport of Diluted Species* to track water vapor
169 diffusion through the air domain and predict the evaporation rate at the droplet surface; and (3) *Heat Transfer in Fluids*
170 which accounts for the non-isothermal flow within the computational domain, temperature-dependent saturation vapor
171 density at the droplet interface, and a boundary heat source to account for the latent heat of evaporation. The
172 computational domain also includes an infinite element air domain (COMSOL 2023b) to specify and maintain
173 boundary conditions far away from the droplet. The physics modules are coupled through non-isothermal flow
174 between heat transfer and fluid flow, and mass transport at the fluid-fluid interface between fluid flow and species
175 transport.

176
177 A non-uniform moving mesh was created by breaking down the computational domain into numerous fine elements
178 of variable sizes, using the Arbitrary Lagrangian-Eulerian technique (Yang et al., 2014) to accurately track the moving
179 air-water interface at the droplet surface. In the ALE technique, the spatial cartesian coordinate system (r, z) is fixed,
180 while the coordinates of the material (R, Z) and the mesh (R_m, Z_m) nodes are functions of time as the droplet evaporates.
181 However, the material and mesh node coordinates are always fixed in their respective frames. Initially, the spatial,
182 material and mesh frames are all identical. As the simulation starts, the material and mesh frames deform as the moving
183 boundary of the droplet shrinks during evaporation. After each time step, the deformed nodes are mapped to the spatial
184 frame, where calculations are performed. In this study, we have used triangular mesh elements (COMSOL 2023c)
185 within the droplet and quadrilateral mesh elements (COMSOL 2023d) for the rest of the domain as shown in Fig. 1.
186 The triangular mesh allows a higher resolution at the droplet surface, and both meshes adjust continually as the droplet
187 surface shrinks during evaporation. Finally, to simulate the water droplet evaporating in ambient air system, with

Deleted: 2

Formatted: Line spacing: At least 15 pt, Font Alignment: Baseline

Deleted: also

Formatted: Font color: Black

Deleted: . The PDEs are discretized and solved along non-uniform moving mesh nodes using the Arbitrary Lagrangian-Eulerian technique (Yang et al., 2014) to accurately track the moving air-water interface at the droplet surface.

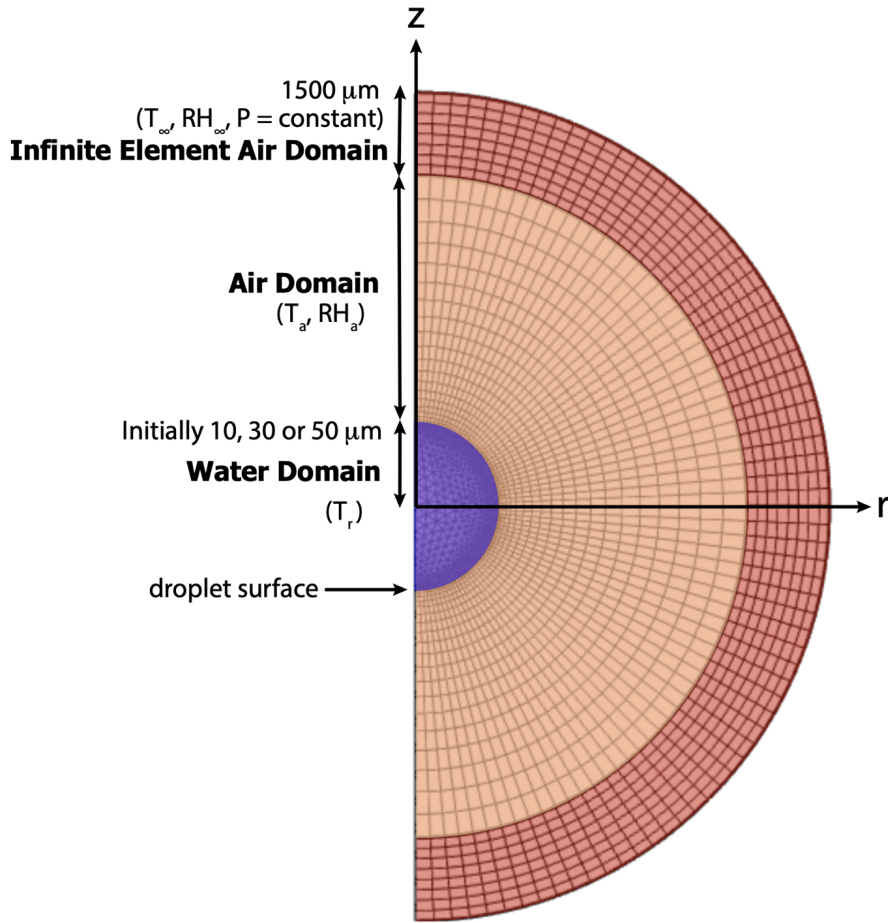
Deleted: ¶
The COMSOL multiphysics software uses cylindrical coordinates (r, ϕ, z) to solve 2D axisymmetric geometries (z -axis is the axis of symmetry), where r represents the radial distance from the longitudinal axis, ϕ is the azimuthal angle (in the interval from $-\pi$ to π), and z is the distance from the origin along the longitudinal axis (COMSOL 2023a). For this modeling scenario, the geometry consists of a 2D axisymmetric domain with the center of the cloud droplet at the origin (defined at $r = 0, z = 0$) with ambient air surrounding the droplet (Fig. 1). The physics interfaces take care of the differential operators while solving the equations arising from the conservation laws.

Formatted: Subscript

Formatted: Subscript

Deleted: ¶

209 appropriate initial and boundary conditions, the discretized PDEs are numerically solved with adaptive time steps (\leq
 210 0.01 s) to maintain numerical stability and obtain the solution (the temporal evolution of droplet temperature and
 211 radius) for a range of conditions.



212
 213
 214 **Figure 1:** Schematic depicting the evaporating droplet, embedded in the air domain. The spatial frame (r, z) and the
 215 initial mesh frame (triangular elements within the droplet and quadrilateral elements outside the droplet) are shown (not
 216 to scale).

Deleted: Computational domain
 Deleted: including the evaporating droplet, embedded in the air domain.

218

222 **2.2 Justification for choice of environmental parameters in the simulations**

223
224 Probing the evolution of the droplet and its immediate environment under a wide swath of conditions was
225 computationally too expensive, thus, certain choices regarding the parameter selection were made. The assumption
226 behind the computational set-up is that the supercooled droplet is suddenly introduced to a subsaturated environment
227 with ambient temperature, $T_\infty = 273.15$ K, 268.15 K, or 263.15 K, as might happen when the droplets are near cloud
228 boundaries such as those occurring in cloud-top generating cells. These temperatures are the ones where activation of
229 INPs is thought to be least effective. Calculations presented in Sec. 4 consider three different environments having
230 ambient relative humidity, $RH_\infty = 10, 40,$ and 70% , and two different ambient pressures, $P = 500,$ and 850 hPa, and
231 initial cloud droplet radii, $r_0,$ of 10, 30, and 50 μm . The pressure levels were chosen based on the occurrence of 273.15
232 K, 268.15 K, and 263.15 K in standard atmospheric profiles for tropical latitudes and middle latitudes under warm
233 and cool season conditions (Standard Atmosphere, 2021). Overall, 90 numerical experiments were performed using
234 various combinations of initial $RH_\infty, T_\infty, P,$ and r_0 to obtain a better understanding of the relationships between the
235 evolution of droplet temperatures and radii, and environmental variables. Of these, the results of 54 experiments are
236 reported in detail herein. The results of these experiments are later summarized in Figs. 3-10 and Tables 1-2. The
237 specific combinations of environmental parameters and initial droplet radii used in this study were also selected to
238 enable easy comparison with results from a previous study of droplet evaporation (Roy et al., 2023). Also, to be noted,
239 the effect of radiation in this study was neglected based on Roy et al. (2023), which demonstrated the negligible role
240 played by radiation in modifying evaporating droplet temperatures under most subsaturated conditions ($RH < 80\%$).

241
242 **2.3 Justification for choice of droplet lifetime cut-off**

243
244 For each experiment, the computational time rose exponentially to maintain numerical stability as the droplet radius
245 decreased during evaporation and the grid sizes needed to be smaller. To avoid exceptionally long computation time,
246 the cut-off radius for the simulations was set to be when the volume of the droplets decreased by 99.5% to reach 0.5%
247 of the initial droplet volume. For $r_0 = 10, 20, 30, 40, 50$ μm , the cutoff radii of the droplets are 1.71, 3.42, 5.13, 6.84,
248 and 8.55 μm , respectively. Note that due to the Raoult effect, for a solution droplet with a mass of dissolved and
249 ionized NaCl = 10^{-13} g, the reduction in the evaporation rate (dr/dt) from that of a pure water droplet is about 1% for
250 a 1 μm radius droplet and 4% for a 0.7 μm droplet. As all cut-off radii considered here are > 1 μm , the solute effect
251 can be neglected. From the Kelvin equation, the equilibrium vapor pressure over a curved surface of pure water
252 approaches the value of equilibrium vapor pressure over a flat surface of pure water for a radius > 0.01 μm . Thus,
253 curvature effects were also neglected. For simplicity, we will refer to the cutoff time as the *droplet lifetime*, although
254 the droplets will survive for a longer time before complete evaporation. The droplet lifetime increases with the initial
255 droplet radius, higher atmospheric pressure, and higher RH_∞ (Fig. 2).

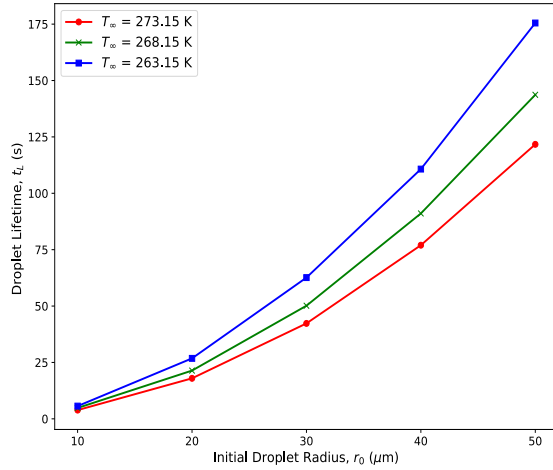
256

Deleted: -

Deleted: 4

Deleted: 4

Deleted: the



261
 262 **Figure 2: Droplet lifetimes, t_L in seconds, for droplets with varying initial droplet radii, $r_0 = 10, 20, 30, 40$ and $50 \mu\text{m}$,**
 263 **evaporating in an initial ambient environment with three different ambient temperatures, $T_\infty = 273.15$ (0°C), 268.15 (-5°C)**
 264 **and 263.15 (-10°C) K, with relative humidity, $RH_\infty = 70\%$, with pressure, $P = 850$ hPa.**
 265

266 **2.4 Sensitivity to domain size**

267
 268 It was important to ensure that the spatiotemporally varying thermal and vapor density gradients in the ambient air in
 269 the vicinity of the evaporating droplet don't interfere with the constant ambient conditions (RH_∞ and T_∞) at the external
 270 boundary of the computational domain. Sensitivity tests with different air domain sizes of 10, 30, and 50 times the
 271 initial droplet radius were carried out to determine the droplet temperature and radial dependence on domain size. It
 272 was found that the evolution of droplet temperature and radius was not sensitive to domain sizes larger than 10 times
 273 the droplet radius considered. Based on the sensitivity analysis, the maximum size of the computational domain for
 274 all experiments was fixed at $1500 \mu\text{m}$, 30 times the largest droplet considered.

275
 276 **3 Theory**

277
 278 **3.1 Assumptions**

279
 280 The framework of the numerical model assumes that an isolated, stationary, spherical, pure water droplet is suspended
 281 within a 2D axisymmetric ambient air domain with constant ambient temperature ($\leq 0^\circ\text{C}$) and relative humidity
 282 ($<100\%$) at a sufficiently far distance away from the droplet that the droplet evaporation does not influence the far
 283 environment. The water droplet and air are considered to be Newtonian fluids, with the assumption that no internal
 284 circulation occurs within the droplet and that there is no ventilation, no radiative heat transfer, and negligible buoyancy
 285 effects due to gravity. This computational approach is an advanced form of the one described in Roy et al., (2023),

286 but also includes the effect of internal droplet heat transfer and spatiotemporal gradients in temperature and vapor
 287 density between the droplet and the environment (see discussion in Sec. 5).

288
 289 **3.2 Governing Equations**
 290

291 Based on the above assumptions, the following are the equations governing the system during droplet evaporation in
 292 the ambient air.

294 (1) Fluid flow: The *Laminar Flow* interface models the weakly compressible form of the Navier-Stokes equation,
 295 along with the continuity equation in the water and air domains,

296
 297
$$\rho \frac{\partial \mathbf{u}}{\partial t} + \rho(\mathbf{u} \cdot \nabla) \mathbf{u} = \nabla \cdot [-p\mathbf{I} + \boldsymbol{\tau}] + \mathbf{F} \quad (1)$$

 298
$$\boldsymbol{\tau} = \mu(\nabla \mathbf{u} + (\nabla \mathbf{u})^T) - \frac{2}{3}\mu(\nabla \cdot \mathbf{u})\mathbf{I} \quad (2)$$

 299
$$\frac{\partial \rho}{\partial t} + \nabla \cdot (\rho \mathbf{u}) = 0 \quad (3)$$

300
 301
$$\frac{\partial \rho}{\partial t} + \nabla \cdot (\rho \mathbf{u}) = 0$$

 302 where t is time, ρ is the fluid density (kg/m^3), \mathbf{u} is the fluid velocity vector (m/s), p is pressure (Pa), \mathbf{I} is the identity
 303 tensor, $\boldsymbol{\tau}$ is the viscous stress tensor (Pa), \mathbf{F} is the external volume force vector (N/m^3), which is assumed to be
 304 negligible here, and μ is the fluid dynamic viscosity. For water below 273.15 K, the dynamic viscosity can be
 305 approximated as 1.79 mPa s. For air, COMSOL uses an empirical equation that produces values equivalent to
 306 Sutherland's law (White, 2006), $\mu = \mu_0 \left(\frac{T}{T_0}\right)^{\frac{3}{2}} \left(\frac{T_0 + S_\mu}{T + S_\mu}\right)$ where $\mu_0 = 1.716 \times 10^{-5} \text{ N s m}^{-2}$, $T_0 = 273 \text{ K}$, and $S_\mu = 111 \text{ K}$
 307 for air. The empirical equation is given as:

308
$$\mu = -8.38278 \times 10^{-7} + 8.35717342 \times 10^{-8}T - 7.69429583 \times 10^{-11}T^2 + 4.6437266 \times 10^{-14}T^3 -$$

 309
$$1.06585607 \times 10^{-17}T^4 \quad (4)$$

311 (2) Heat Transport: The *Heat Transfer in Fluids* interface models heat transfer in all domains (air, water, infinite
 312 element domain) using the following version of the heat equation:

313
 314
$$\rho C_p \frac{\partial T}{\partial t} + \rho C_p \mathbf{u} \cdot \nabla T + \nabla \cdot \mathbf{q} = 0 \quad (5)$$

 315
$$\mathbf{q} = -k \nabla T \quad (6)$$

316
 317 where ρ (kg/m^3) is the fluid density, C_p ($\text{J}/(\text{kg} \cdot \text{K})$) is the fluid heat capacity at constant pressure, T is the temperature,
 318 k ($\text{W}/(\text{m} \cdot \text{K})$) is the fluid thermal conductivity, \mathbf{u} (m/s) is the fluid velocity field from the *Laminar Flow* interface, \mathbf{q}
 319 (W/m^2) is the heat flux by conduction. We chose the value of k for supercooled water at $0.56 \text{ W m}^{-1} \text{ K}^{-1}$ based on Fig.

Moved (insertion) [1]
 Formatted: Font: Cambria Math
 Formatted: Font: Cambria Math, Not Bold
 Formatted: Font: Cambria Math
 Formatted: Tab stops: 2.31", Left + 6", Right
 Moved up [1]: $\rho \frac{\partial \mathbf{u}}{\partial t} + \rho(\mathbf{u} \cdot \nabla) \mathbf{u} = \nabla \cdot [-p\mathbf{I} + \boldsymbol{\tau}] + \mathbf{F}$
 Deleted: $\rho \frac{\partial \mathbf{u}}{\partial t} + \rho(\mathbf{u} \cdot \nabla) \mathbf{u} = \nabla \cdot [-p\mathbf{I} + \boldsymbol{\tau}] + \mathbf{F}$
 Deleted: I
 Formatted: Font: Not Bold
 Formatted: Font: Not Italic
 Formatted: Font: Cambria Math, Italic
 Formatted: Font: Cambria Math
 Formatted: Font: Cambria Math, Not Bold, Not Italic
 Formatted: Font: Cambria Math
 Moved (insertion) [2]
 Formatted: Font: Not Italic
 Formatted: Indent: Left: 0.5"
 Formatted: Font: Not Bold
 Formatted: Tab stops: 2.31", Left + 6", Right
 Moved up [2]: $\frac{\partial \rho}{\partial t} + \nabla \cdot (\rho \mathbf{u}) = 0$
 Formatted: Font: Italic
 Formatted: Font: Cambria Math, Italic
 Deleted: μ is the fluid dynamic viscosity,
 Formatted: Indent: Left: 0.5", Tab stops: 2.31", Left + 6", Right
 Deleted: ∇
 Deleted: ∇
 Formatted: Tab stops: 2.31", Left + 6", Right
 Deleted: Q_b
 Deleted: ∇
 Formatted: Font: Not Italic
 Formatted: Font: Not Italic
 Formatted: Font: Not Bold
 Formatted: Font: Not Bold
 Formatted: Font: Not Bold
 Formatted: Tab stops: 2.31", Left + 6", Right
 Formatted: Font: Italic

329 3 of Biddle et al., (2013) where the thermal conductivity of supercooled water is very close to 0.56 W/(m K) for the
 330 range of temperatures used in this study. Based on Beard and Pruppacher (1971), the thermal conductivity of air, given
 331 by $k_a = 0.004184[5.69 + 0.017(T - 273.15)]$ (W m⁻¹ K⁻¹), has very weak dependence on temperature over the
 332 temperature range used in this study. For both T = 273.15 K and 253.15 K, the value of k_a is 0.02 W m⁻¹ K⁻¹. Hence,
 333 we have used a constant value of 0.02 W m⁻¹ K⁻¹.

Deleted: , and Q_b (W/m³) is the heat sink due to evaporative cooling at the droplet surface.

335 (3) **Mass transport:** The *Transport of Diluted Species* interface models water vapor transport through Fick's laws of
 336 diffusion, solving the mass conservation equation for vapor transfer in all domains except within the cloud droplet:

338
$$\frac{\partial c}{\partial t} + \nabla \cdot \mathbf{J} = 0 \quad (7)$$

Formatted: Font: Not Italic

339
$$\mathbf{J} = -D\nabla c \quad (8)$$

Formatted: Tab stops: 2.31", Left + 6", Right

Deleted: ¶

340 where c is the concentration of water vapor (mol/m³), D denotes the diffusion coefficient (m²/s), and \mathbf{J} is the mass flux
 341 diffusive flux vector (mol/(m²·s)). D is calculated following Hall and Pruppacher (1976) and defined as follows: $D =$
 342 $0.0000211 \frac{P_0}{P} \left[\frac{T}{T_0} \right]^{1.94}$ (m² s⁻¹) with reference pressure, $P_0 = 1013.25$ hPa, reference temperature, $T_0 = 273.15$ K,
 343 atmospheric temperature, T , and pressure, P . In this study, values of P are either fixed at 500 or 850 hPa to determine
 344 the effect of ambient air pressure on droplet evaporation. \mathbf{J} is obtained from the Laminar Flow interface through
 345 coupling between these interfaces.
 346

Formatted: Font: Not Bold

Formatted: Justified, Tab stops: 2.31", Left + 6", Right

Formatted: Tab stops: 2.31", Left + 6", Right

348 **3.3 Initial conditions**

349 The initial velocity components in the r , and z directions are assumed to be 0 m/s in both air and water domains. The
 350 initial fluid pressure is $p = P_{0,air}$ (Pa), specified either at 500 or 850 hPa in the air domain, and in the water domain, p
 351 $= P_{0,water} = \frac{2\sigma}{r_0}$ Pa, where surface tension, $\sigma = 70 \times 10^{-3}$ (N/m). For the heat transfer module, all domains are assumed
 352 to be at a prescribed initial ambient temperature, T_0 , which is the same as that of a point at a far distance away from
 353 the droplet, T_∞ .

Deleted: ¶

354 For the vapor transfer interface, except within the droplet, all domains are at an initial vapor concentration of $c_{0,air}$
 355 which is again assumed to be the same as that of the constant ambient concentration value far from the droplet, c_∞ ,
 356 calculated as follows:

Formatted ... [1]

Formatted ... [2]

Formatted ... [3]

Formatted ... [4]

Formatted ... [5]

Formatted ... [6]

Formatted ... [7]

357 $c_\infty = \frac{RH_\infty \times e_{sT_\infty}}{R_{univ} \times T_\infty}$ where, RH_∞ is set at a constant ambient relative humidity far from the droplet, $R_{univ} = 8.3145$
 358 (J/mol/K), T_∞ is in K. The saturation vapor pressure is calculated as, $e_{sT_\infty} = 610.94 * \exp\left(\frac{17.625 * T_\infty}{T_\infty + 243.04}\right)$ (in Pa, with
 359 T_∞ in °C) following Alduchov and Eskridge (1996).

Deleted: For the vapor transfer interface, except within the droplet, all domains are at an initial vapor concentration of $c_{0,air}$ which is again assumed to be the same as that of the constant ambient concentration value far from the droplet, c_∞ , calculated as follows:
 $c_\infty = \frac{RH_\infty \times e_{sT_\infty}}{R_{univ} \times T_\infty}$ where, RH_∞ is set at a constant ambient relative humidity far from the droplet, $R_{univ} = 8.3145$ (J/mol/K) and saturation vapor pressure, $e_{sT_\infty} = 610.94 * \exp\left(\frac{17.625 * T_\infty}{T_\infty + 243.04}\right)$ (in Pa, with T_∞ in °C) following Alduchov and Eskridge (1996).

389

3.4 Model Constraints and Boundary Conditions

390

391 1. Within the droplet and throughout the domain, the following conditions are applicable:

$$392 \mathbf{u} \cdot \mathbf{n} = 0 \tag{9}$$

$$393 [-p\mathbf{I} + \boldsymbol{\tau}] \cdot \mathbf{n} = 0 \tag{10}$$

$$394 \mathbf{q} \cdot \mathbf{n} = -k\nabla T \cdot \mathbf{n} = 0 \tag{11}$$

$$395 -D\nabla c \cdot \mathbf{n} = 0 \tag{12}$$

396 where \mathbf{n} is the normal to an outward-pointing vector from the center of the droplet. This constraint limits water
397 mass, water vapor and heat flow to the direction normal to the droplet surface.

400 2. At the fluid-fluid interface i.e., droplet-air boundary, the droplet surface is assumed to be at vapor saturation
401 throughout its lifetime. Hence, saturated vapor concentration at the shrinking droplet boundary, using the ideal gas

402 law, is given by, $c_{sat}(T_{sf}) = \frac{e_s(T_{sf})}{R_{air} M_{air} T_{sf}}$ where T_{sf} is the surface temperature, in K. The saturation vapor pressure $e_s(T_{sf})$
403 is estimated as $e_s(T_{sf}) = 610.94 * \exp\left(\frac{17.625 * T_{sf}}{T_{sf} + 243.04}\right)$ (in Pa, with T_{sf} in °C) again following Alduchov and Eskridge
404 (1996).

405 The local evaporative mass flux at the interface is given by diffusion of water vapor across the water-air interface, M_j
406 (kg/ m² s)

$$407 M_j = M_w \mathbf{n} \cdot (-D\nabla c) \tag{13}$$

408 where the molecular weight of water, $M_w = 0.018$ (kg/mol). Although the temperature is continuous across the droplet-
409 air boundary, there is a discontinuity in heat flux across the interface due to the evaporation of water. Thus, the latent
410 heat of evaporation L , defined as $L = [2501 - 2.44T_r]$ kJ kg⁻¹ with droplet surface temperature, T_r in °C, is
411 incorporated as a boundary heat sink as $-M_j L$ (W/m²).
412
413

414 The mass balance at the water-vapor boundary at the droplet surface, and the velocity of the moving mesh \mathbf{u}_{mesh} , at
415 the shrinking water-air interface, are expressed by the following equations, based on Scardovelli and Zaleski, (1999):
416
417

$$418 \mathbf{u}_w = \mathbf{u}_v + M_j \left(\frac{1}{\rho_w} - \frac{1}{\rho_v} \right) \mathbf{n} \tag{14}$$

$$420 \mathbf{u}_{mesh} = (\mathbf{u}_w \cdot \mathbf{n} - \frac{M_j}{\rho_w}) \mathbf{n} \tag{15}$$

421 where the subscripts w and v represent water and vapor respectively.
422
423

Deleted: At the center of ...he droplet and throughout the domainmain... $r=0$,...axisymmetric ...he following conditions are applicable:¶ ... [8]

Formatted: Justified, Tab stops: 2.31", Left + 6", Right

Formatted: Font: Not Bold

Formatted: Font: Not Bold

Deleted: surface normal vector.

Formatted: Justified, Space Before: 0 pt, After: 0 pt, Line spacing: 1.5 lines

Deleted: T

Deleted: T

Deleted: where saturation vapor pressure,

Deleted: T , ...s estimated as following Alduchov and Eskridge (1996) at $T = T_{sf}$, the temperature at the droplet surface (in °C). ... [11]

Formatted ... [9]

Formatted ... [10]

Formatted: Font color: Text 1

Formatted ... [12]

Formatted ... [13]

Deleted: ¶

Formatted: Tab stops: 2.31", Left + 6", Right

Formatted: Font: Bold, Not Italic

Formatted ... [14]

Formatted ... [15]

Formatted: Tab stops: 2.31", Left + 6", Right

Formatted ... [16]

453 The stresses are balanced at the water-vapor interface by the following conditions, based on Yang et al., (2014):

454

$$455 \quad \mathbf{n} \cdot (\mathbf{S}_w - \mathbf{S}_v) = \sigma(\nabla_\sigma \cdot \mathbf{n})\mathbf{n} - \nabla_\sigma \sigma \quad (16)$$

456

$$457 \quad \mathbf{S} = [-p\mathbf{I} + \boldsymbol{\tau}] \quad (17)$$

458 where \mathbf{S} is the total stress tensor and ∇_σ is the surface gradient operator defined by

459

$$460 \quad \nabla_\sigma = (\mathbf{I} - \mathbf{n} \cdot \mathbf{n}^T)\nabla \quad (18)$$

462 In the normal direction of the boundary, the force is balanced by,

463

$$464 \quad \mathbf{n} \cdot (\mathbf{S}_w - \mathbf{S}_v) = \frac{\sigma}{r_c} \cdot \mathbf{n} \quad (19)$$

465 where r_c is the curvature radius.

466 3. The external air domain boundary is open with the following condition:

469

$$470 \quad [-p\mathbf{I} + \boldsymbol{\tau}]\mathbf{n} = -f_0\mathbf{n}_e \quad (20)$$

471 where normal stress, $f_0 = 0 \text{ N/m}^2$.

472 4. The infinite element domain consists of air and is considered to be an ideal gas. The temperature, relative humidity,
473 and concentration far from the droplet i.e., at the inner boundary of the infinite element domain, are fixed at T_∞ and
474 c_∞ , respectively.

476 3.5 Coupling between the COMSOL interfaces

477

478 To numerically model the evaporating droplet embedded in the air domain, intercoupling between the three physics
479 interfaces - laminar two-phase flow (formulated within the Arbitrary Lagrangian-Eulerian framework), the heat
480 transfer in fluids, and the transport of diluted species within the air medium are established through the following
481 mechanisms: (i) the local evaporative mass flux at the droplet-air interface, which is related to the mesh velocity for
482 the laminar flow, is estimated by the diffusion of water vapor in the air domain; (ii) saturated vapor concentration at
483 the droplet-air interface, which serves as a boundary condition for the vapor diffusion, is calculated using the local
484 temperature at the droplet interface; and (iii) the evaporative heat flux at the droplet-air interface acts as a heat sink
485 boundary condition for the heat transfer in fluids module.

487 4 Results

488 4.1 Internal Droplet Temperature Evolution

Deleted: following

Formatted: Adjust space between Latin and Asian text, Adjust space between Asian text and numbers, Tab stops: 2.31", Left + 6", Right

Formatted: Font: Not Bold

Formatted: Font: Bold

Formatted: Adjust space between Latin and Asian text, Adjust space between Asian text and numbers, Tab stops: 2.31", Left + 6", Right

Formatted: Font: Not Bold

Formatted: Font: Not Bold

Formatted: Font: Bold

Formatted: Font: Not Bold

Formatted: Font: Not Bold

Formatted: Font: Bold

Formatted: Font: Not Bold

Formatted: Tab stops: 2.31", Left + 6", Right

Deleted: ¶

Deleted: ¶

4.1 Internal Droplet Temperature Evolution¶

493 Since evaporation is a surface phenomenon, with the evaporative cooling at the droplet surface acting as a heat sink,
 494 the temperature of the evaporating droplet surface should be lower than the center of the droplet. In all simulations,
 495 the center to surface temperature gradient within the droplet forms almost instantaneously as evaporative cooling at
 496 the droplet surface occurs extremely fast. The time required for the droplet to reach internal thermal equilibrium
 497 depended slightly on the initial size of the droplet and the ambient RH_∞ , with larger droplets and drier environments
 498 leading to more time required by the droplets to reach equilibrium. However, generally, for typical cloud droplet sizes
 499 and environmental conditions considered here ($r_0 = 10, 30, 50 \mu\text{m}$), the internal thermal gradients dissipate and the
 500 temperatures throughout the droplets become uniform in $\leq 0.3 \text{ s}$, consistent with Fick's laws of diffusion with a
 501 diffusive timescale of r^2/D , where r is the length scale and D is the thermal diffusivity of water. For this study, we
 502 have simulated internal droplet heat transfer for the entirety of the droplet lifetime and will be reporting the average
 503 droplet temperatures as "droplet temperatures" in the results, unless noted otherwise.

4.1 Droplet Thermal and Radial Evolution: Influence of Initial Droplet Size and Environmental Factors

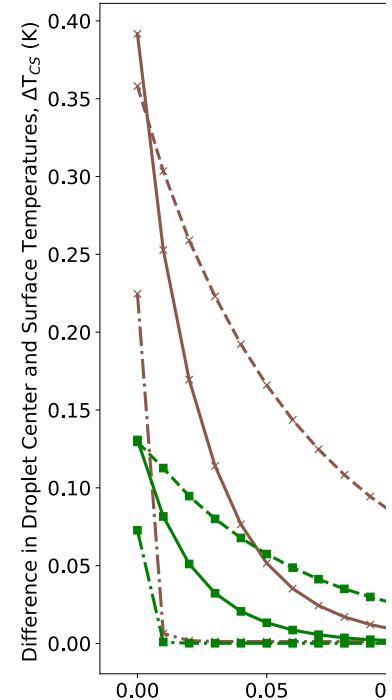
508 Figures 3 and 4 depict the early evolution of the droplet average temperatures and radii ($r_0 = 10, 30$ and $50 \mu\text{m}$) for
 509 the first few seconds of their lifetimes (as defined in Sec. 2c), for different environments with constant ambient
 510 conditions (T_∞, RH_∞ , and P) far from the droplet. Tables 1 and 2 provide the final temperature values and total lifetimes
 511 of the droplets. Figures 3 and 4 also state the droplet temperatures at the end of their lifetimes (T_L) and the total
 512 lifetimes of the droplets (t_L). For all numerical experiments, the evaporating droplet temperature decreases sharply,
 513 within $< 0.5 \text{ s}$, to a certain temperature defined here as the transition point, T_i , where the slope of the curve changes.
 514 After reaching T_i , the decrease in droplet temperature is relatively more gradual as can be seen from Figs. 3 and 4. For
 515 example, in Fig. 3(c), for $P = 500 \text{ hPa}$, $T_\infty = 268.15 \text{ K}$ (-5°C), $RH_\infty = 10\%$, a droplet with $r_0 = 10 \mu\text{m}$, takes about 0.03
 516 s to reach T_i at 260.98 K (a decrease of 7.17 K from initial temperature). In contrast, a $30 \mu\text{m}$ droplet takes about 0.12
 517 s to reach T_i at 260.85 K (a decrease of 7.3 K from initial temperature), and a $50 \mu\text{m}$ droplet takes about 0.33 s to
 518 reach T_i . Finally, the $10 \mu\text{m}$ droplet reaches the end of its lifetime in 1.05 s i.e. $t_L = 1.05 \text{ s}$ with temperature, $T_L =$
 519 244.12 K after reaching T_i , while for the $30 \mu\text{m}$ droplet, $t_L = 11.4 \text{ s}$ with $T_L = 244.31 \text{ K}$, and $t_L = 32.76 \text{ s}$ for the $50 \mu\text{m}$
 520 droplet with $T_L = 244.29 \text{ K}$ after reaching T_i .

522 The evaporation process in these experiments starts in a condition that is far from equilibrium. The coupled air- droplet
 523 system attempts to evolve towards a steady-state where the thermal energy towards the droplet compensates for
 524 evaporative cooling at the droplet surface. In this process, the droplet initially rapidly cools to the thermodynamic
 525 wet-bulb temperature of the initial environment similar to what has been shown in Roy et al., (2023). However, under
 526 low relative humidity conditions, the thermal and vapor diffusion are not yet near equilibrium. As the system attempts
 527 to achieve a steady-state, the imbalance in the heat fluxes associated with vapor and thermal diffusion in the immediate
 528 vicinity of the drop leads to a gradual reduction in the wet-bulb temperature of the immediate droplet environment
 529 leading to a continued slow decrease in the droplet temperature as the droplet continues to evaporate.

Deleted: This is indeed the case, as shown in the examples in Fig. 3, where 10, 30 and 50 μm droplets are evaporating in two types of environments: very dry ($RH_\infty = 10\%$) and relatively moist ($RH_\infty = 70\%$), with $P = 500 \text{ hPa}$, and $T_\infty = 273.15 \text{ K}$n all simulations, tNote that t...e center to surface temperature gradient within the droplet forms almost instantaneously ($< \text{smallest output timestep of } 0.01 \text{ s}$) ...s evaporative cooling at the droplet surface occurs extr... [17]

Deleted: This can be explained by the high thermal conductivity values of water (assumed constant at 0.556 W/(m K)) and the absence of any heat source within the droplet.

Formatted: Superscript



Deleted: ... [18]

Deleted: 2

Deleted: ... 34... and 45... depict the early evolution of the droplet average temperatures and radii ($r_0 = 10, 30$ and $50 \mu\text{m}$) for the first few 10...seconds of their lifetimes (as defined in Sec. 2c), for different environments with constant ambient conditions (T_∞, RH_∞ , and P) far from the droplet. Tables 1 and 2 provide the final temperature values and total lifetimes of the droplets. These ...f... gures 3 and 4 also state the visually summarize ...roplet temperatures at the e... [19]

Moved down [3]: In general, we can see that a higher ambient T_∞ , and lower RH_∞ and P leads to a larger reduction in droplet temperature from its initial temperature. Therefore, drier, relatively warmer (closer to 0°C), and lower-pressure environments lead to the strongest evaporative cooling of the droplets. Also, due to evaporative cooling, the droplets survive longer as compared to the pure diffusion-limited evaporation approach where the decreases in evaporating

689 In general, we can see that a higher ambient T_∞ and lower RH_∞ and P leads to a larger reduction in droplet temperature
690 from its initial temperature. Therefore, drier, relatively warmer (closer to 0°C), and lower-pressure environments lead
691 to the strongest evaporative cooling of the droplets. Also, due to evaporative cooling, the droplets survive longer as
692 compared to the pure diffusion-limited evaporation approach where the decreases in evaporating droplet temperature
693 have not been considered (see Sec. 5). However, drier, relatively warmer (close to 0°C), and lower-pressure
694 environments lead to smaller droplet lifetimes as compared to more humid environments, with lower ambient
695 temperatures and higher pressures.

Moved (insertion) [3]

697 **4.2 Environmental Evolution: Evolution of Temperature, Relative Humidity, and Wet-Bulb Temperature in** 698 **the air domain near the droplet**

Deleted: ¶

700 Figures. [S-7](#)(a, d) show radial cross sections of the computational domain, starting from the center of the droplet at
701 $(r, z) = (0, 0)$, along the r axis to the edge of the domain at $r = 1500 \mu\text{m}$, while Figs. [S-7](#)(b, e) expand the dashed box
702 regions of Figs. [S-7](#)(a, d), and Figs. [S-7](#)(c, f) further expand the dashed box regions of Figs. [S-7](#)(b, e). All panels
703 show the spatiotemporal evolution of temperature (Fig. 5), relative humidity (Fig. 6), thermodynamic wet-bulb
704 temperature (Fig. 7), and droplet radius for a droplet with initial radius, $r_0 = 50 \mu\text{m}$, introduced to an initial environment
705 with pressure, $P = 500 \text{ hPa}$, ambient temperature, $T_\infty = 268.15 \text{ K}$ (-5°C), with two different relative humidities, RH_∞
706 $= 10\%$ and 70% . The evolution of temperature within the droplet is left of the dashed black line, which denotes the
707 droplet radius.

Deleted: 3

Deleted: A

Deleted: 6

Deleted: 8

Deleted:

Deleted: on

Deleted: the origin of x

Deleted: $= 0 \mu\text{m}$

Deleted: x

Deleted: 6

Deleted: 8

Deleted: 6

Deleted: 8

Deleted: 6

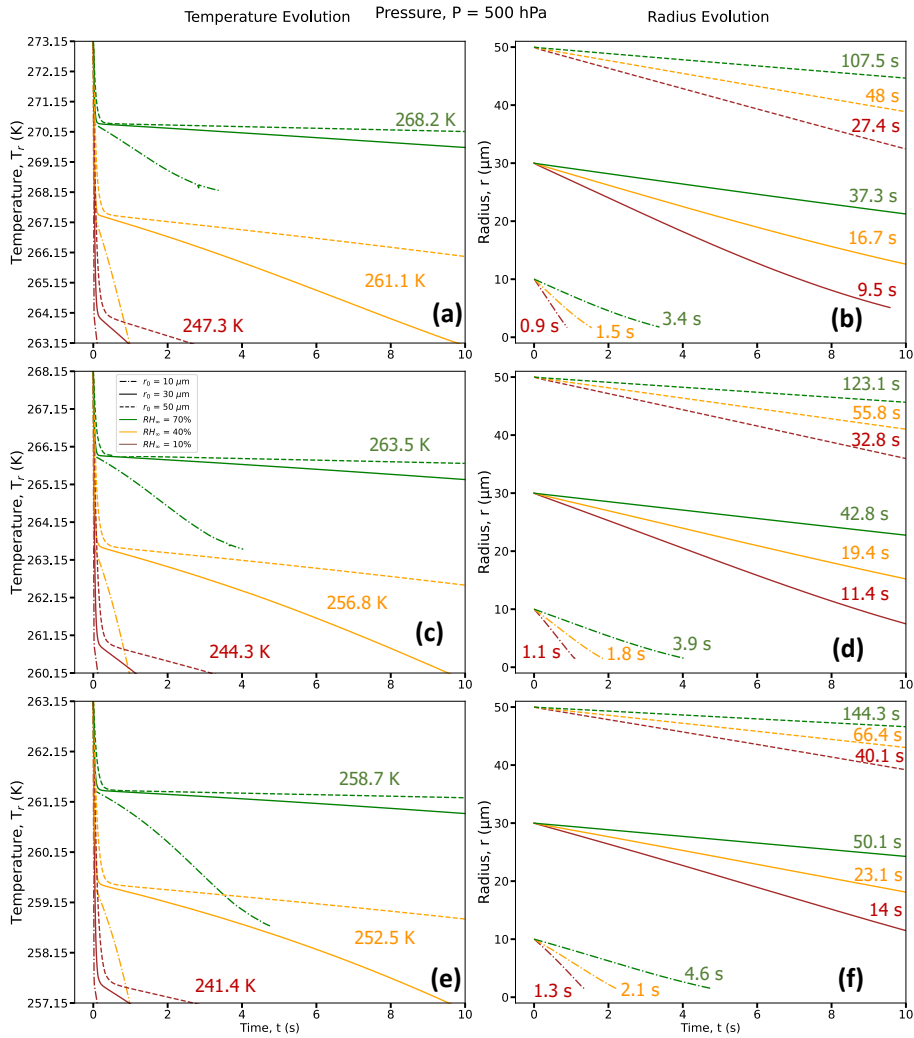
Deleted: 8

Deleted: 6

Deleted: 8

709 As the droplet evaporates in the subsaturated domain, evaporative cooling occurs at the droplet surface, leading to
710 heat transfer both from within the warmer droplet and the surrounding air to balance the cooling at the droplet surface.
711 Since the droplet has no constant internal heat source, the internal thermal gradients dissipate quite fast (within 0.3 s)
712 and the average droplet temperatures continue to decrease as the droplet evaporates. Due to heat exchange between
713 the droplet surface and the ambient air in its vicinity, transient thermal gradients in the ambient air develop and lead
714 to a decrease in the air temperature near the droplet. As the droplet shrinks in size along with cooling further, the
715 colder envelope of air surrounding the droplet shrinks as well and the ambient air far from the droplet, at a constant
716 temperature, acts as a heat source and supplies heat to the rest of the domain to attempt to equilibrate the air
717 temperature. Comparing Fig. [S-7](#)(a) and (d), at the lower RH_∞ , the magnitude of evaporative cooling is much higher.
718 For example, the average temperature of the $50 \mu\text{m}$ droplet decreases by $\sim 10 \text{ K}$ in 9 s when $RH_\infty = 10\%$, while the
719 decrease is $\sim 5 \text{ K}$ in 120 s, when $RH_\infty = 70\%$.

Deleted: 6

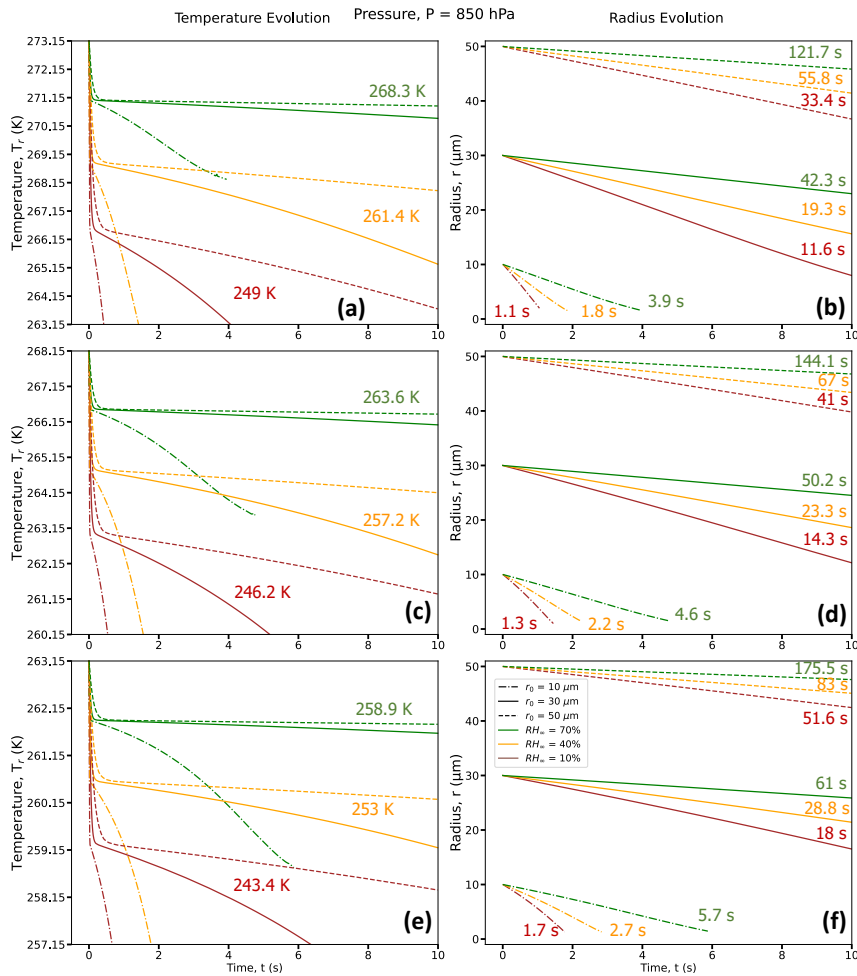


739
740

741 **Figure 3:** Droplet temperature evolution (left column) and radius evolution (right column) for three different RH_∞ ($RH_\infty =$
 742 10% (brown curves), 40% (orange curves) and 70% (green curves)), three different r_0 ($r_0 = 10 \mu\text{m}$ (dot-dashed lines), 30
 743 μm (solid lines) and 50 μm (dashed lines)), with three different $T_\infty = 273.15 \text{ K}$ (0°C) (a, b), 268.15 K (-5°C) (c, d) and 263.15
 744 K (-10°C) (e, f), for $P = 500 \text{ hPa}$. For each RH_∞ , the average droplet temperature at the end of the lifetimes of the three
 745 droplets with different r_0 (T_L , in K) is given in (a,c,e) and the time taken to reach the end of its lifetime (t_L , in s) is given in
 746 (b, d, f). Exact values of final temperature for each r_0 are given in Table 1.

Deleted: 4

Deleted: its



749

750 **Figure 4:** Same as Fig. 3 but for $P = 850$ hPa.

751

752 In these simulations, the air in contact with the droplet surface is saturated with respect to water, i.e., $RH = 100\%$ (Fig.

753 6, a-f), consistent with assumptions of isolated, stationary evaporating droplets (Kinzer and Gunn, 1951; Srivastava

754 and Coen, 1992). As the water vapor from the evaporating droplet surface diffuses into the surrounding environment,

755 with an initial RH (same as RH_{∞}) of say 10%, vapor density gradients, similar to the thermal gradients, appear and

756 impact the immediate environment of the droplet. These spatiotemporally varying thermal and vapor density gradients

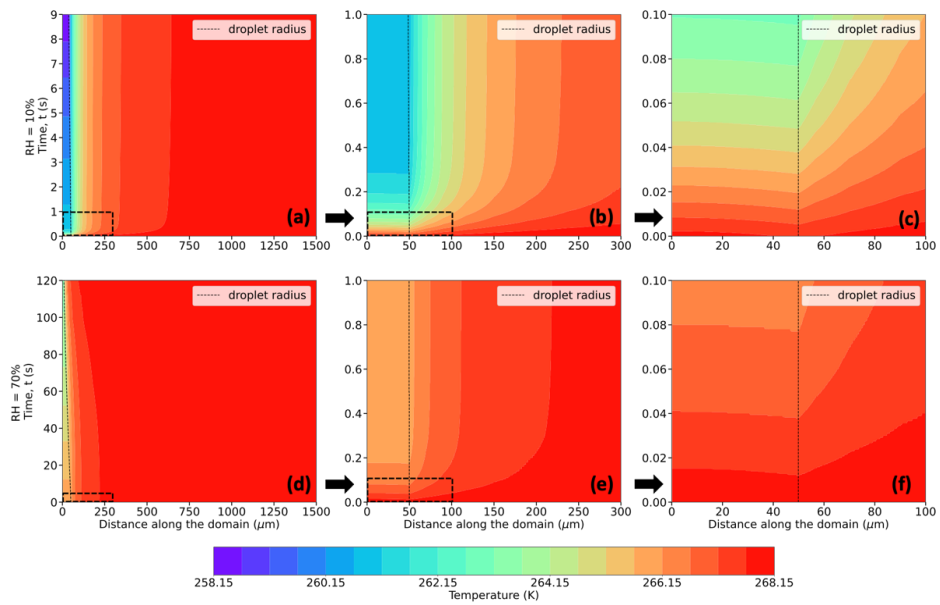
757 play an important role in affecting the droplet temperatures, evaporation rates, and in turn, droplet lifetimes.

Deleted: 5

Formatted: Indent: First line: 0"

Deleted: 7

Deleted: ¶



761
 762 **Figure 5: Evolution of temperature (in K, shaded contours), and droplet radius (in μm, dashed black trace) for a 50 μm**
 763 **droplet, immersed in an environment with $T_{\infty} = 268.15$ K (-5°C), $P = 500$ hPa, and $RH_{\infty} = 10\%$ (top row) and 70% (bottom**
 764 **rows). Bottom left corner of each plot refers to the center of the droplet at $(r, z) = (0, 0)$. Distance along the domain refers**
 765 **to the radial distance from the center of the droplet. Figures denoted as (b) and (e), and (c) and (f) present zoomed-in plot**
 766 **areas marked by the dashed boxes in (a) and (d), and (b) and (e), respectively.**

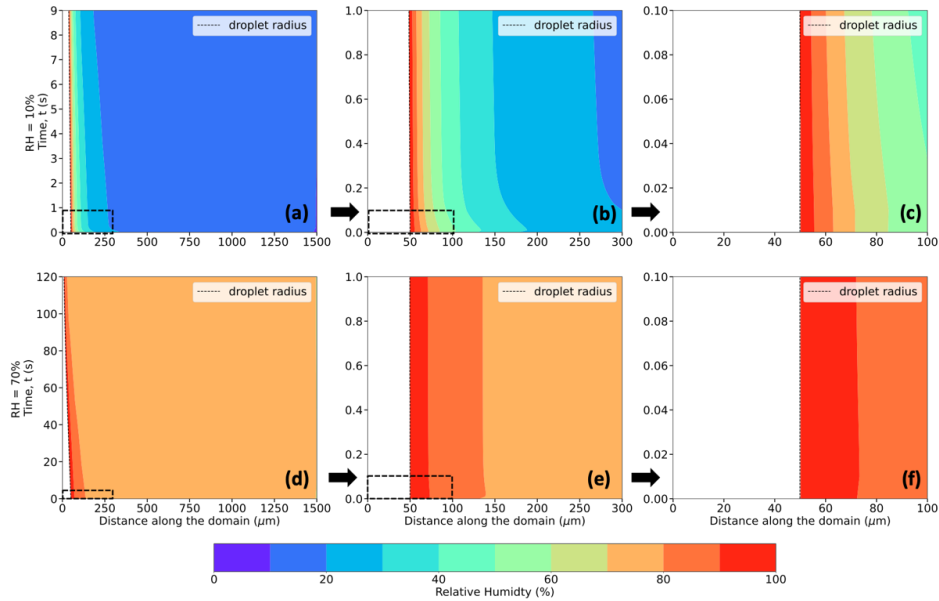


Figure 6: Same as Figure 5, but for Relative Humidity (in %, shaded contours), instead of Temperature.

Roy et al. (2023) has shown that an evaporating cloud droplet temperature can be well-approximated by the thermodynamic wet-bulb temperature of the environment, especially at higher relative humidities and pressures, and lower ambient temperatures. Following the iterative procedure used in Roy et al. (2023) to calculate the thermodynamic wet-bulb temperature (T_{WB}), Fig. 7 (a-f) depicts the evolution of T_{WB} of the surrounding environment. Unlike previous studies (Srivastava and Coen, 1992; Roy et al., 2023), the ambient environment in this study is not assumed to be spatiotemporally invariant. Hence, as the thermal and vapor density gradients evolve in the ambient air, the T_{WB} of the environment evolves as well, depending on the temperature, relative humidity, and pressure, with the droplet surface temperature the same as that of the T_{WB} of its immediate environment at all times. Of interest, the droplet temperature decreases very quickly to T_i within < 0.5 s (Figs. 3 and 4), which agrees very well with the initial T_{WB} of the surrounding environment and the constant value of the thermodynamic wet bulb temperature far from the droplet ($T_{WB\infty}$). For example, in Fig. 7 (a-c), $T_\infty = 268.15$ K, $P = 500$ hPa, $RH_\infty = 10\%$, $T_{WB\infty} = 261.64$ K, and in Fig. 7 (d-f), for $RH_\infty = 70\%$, $T_{WB\infty} = 266.13$ K. Fig. 7 shows the two phases of the evolution of T_{WB} of the immediate environment for two RH_∞ environments – initially, there is a very fast decrease of the air temperature at the droplet surface to $T_{WB\infty}$ typically within < 0.3 s, and then a more gradual decrease of T_{WB} at the droplet surface as the thermal and vapor density gradients in the ambient air become relatively steadier and more established for a period of time, and as their spheres of influence start shrinking as the droplet starts getting smaller in size.

Deleted: 8

Deleted: 4

Deleted: 5

Deleted: 8

Deleted: 8

Deleted: 8

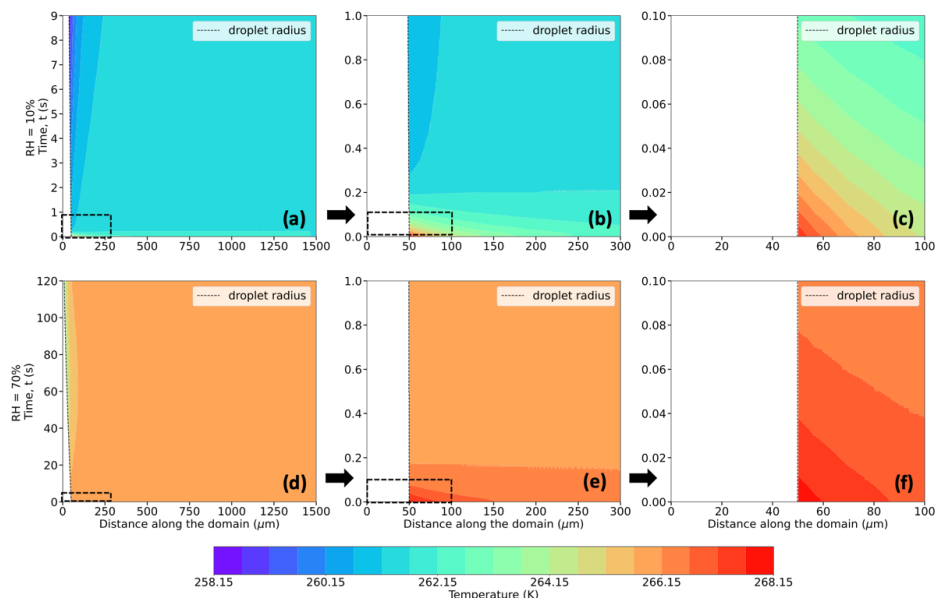


Figure 7: Same as Figure 5, but for thermodynamic wet-bulb temperature (in K, shaded contours).

4.3 Influence of initial droplet size and ambient environmental factors on the thermal evolution of the droplet and its surrounding environment

The overall results spanning the parameter space of the simulations are summarized in Tables 1-2 for the 54 numerical experiments using various combinations of ambient conditions (RH_∞ , T_∞ , and pressure, P , and r_0) specified at a distance far away from the droplet.

4.3.1 Effect of Ambient Relative Humidity, RH_∞

The decrease in droplet temperature is larger when the RH_∞ is lower due to higher evaporation rates and stronger evaporative cooling under drier conditions. For instance, as shown in Table 1 and Fig. 8 (a, b, c), 30 μm droplets reach ~ 247.3 K (a decrease of 25.8 K from the initial temperature of 273.15 K) for $RH_\infty = 10\%$, ~ 261.1 K (a decrease of 12.1 K) for $RH_\infty = 40\%$ and ~ 268.2 K (a decrease of ~ 5 K) for $RH_\infty = 70\%$. The droplet lifetimes vary depending on RH_∞ , with lifetimes increasing with an increase in humidity. For example, the droplet lifetimes for the 30 μm droplet are ~ 9.5 s, 16.7 s, and 37.3 s for environments with $RH_\infty = 10\%$, 40% and 70%, respectively (Table 2). The decrease in droplet temperature and increase in droplet lifetime show similar dependence with increasing RH_∞ for 10 and 50 μm droplets as well.

Deleted: 4

Deleted: o capture t

Deleted: trends

Deleted: most of

Deleted: ,

Deleted: Figs. 9-14 and

Deleted: summarize the results from

Deleted: ,

Formatted: Font color: Blue

Deleted: 4.

Deleted: 9

Deleted: widely

824 **4.3.2 Effect of Initial Droplet Size, r_0**

825
826 From Figs. 8-10, for a given initial environmental condition (RH_∞ and T_∞), the droplet temperatures at the end of their
827 lifetimes are independent of the initial droplet sizes. For example, from Table 1 and Fig. 9(a-i) at $P = 500$ hPa, 10,
828 30 and 50 μm droplets reach ~ 244 K (a decrease of ~ 24 K from the initial temperature of 268.15 K) for $RH_\infty = 10\%$,
829 ~ 256.8 K for $RH_\infty = 40\%$, and ~ 263.5 K for $RH_\infty = 70\%$. On the other hand, the droplet lifetime strongly depends on
830 the initial droplet size, as the larger droplets take more time to evaporate as compared to the smaller ones. For
831 environments with $RH_\infty = 10\%$, 40% and 70%, the droplet lifetimes for the 10 μm droplet are ~ 1.1 s, 1.8 s, and 3.9 s,
832 while for the 30 μm droplet are ~ 11.4 s, 19.4 s, and 42.8 s, and for the 50 μm droplet are ~ 32.8 s, 55.8 s, and 123.1
833 s, respectively (Table 2). For a higher pressure of $P = 850$ hPa (Table 1), at the same T_∞ , irrespective of r_0 , the decrease
834 in droplet temperatures is slightly smaller as compared to $P = 500$ hPa, with values of 22 K, 11 K, and 4.6 K. The
835 radial dependence of the thermal gradients in the ambient air also depends on the initial droplet size, decreasing with
836 a decrease in r_0 .

838 **4.3.3 Effect of Ambient Temperature, T_∞**

839
840 To determine the effect of a lower ambient temperature on droplet temperatures and lifetimes, Figs. 9 and 10
841 demonstrate similar plots as shown in Fig. 8, but for $T_\infty = 268.15$ K (-5°C) and 263.15 K (-10°C), respectively. The
842 decrease in droplet temperatures and increase in droplet lifetimes depict similar relationships with RH_∞ and r_0 .
843 Droplets, irrespective of their initial size, cool to a lower temperature depending on the ambient RH_∞ , with the
844 magnitude of the cooling being inversely proportional to the subsaturation of the ambient environment. For instance,
845 for 10, 30 and 50 μm droplets, from an initial temperature of 268.15 K, the droplet temperatures approximately
846 decrease by 24 K, 11.4 K, and 4.7 K, for environments with $RH_\infty = 10\%$, 40%, and 70%, respectively (Table 1). The
847 droplet lifetimes for the 10 μm droplet are ~ 1.1 s, 1.8 s, and 3.9 s, while for the 30 μm droplet are ~ 11.4 s, 19.4 s,
848 and 42.8 s, and for the 50 μm droplet are ~ 32.8 s, 55.8 s, and 123.1 s, for $RH_\infty = 10\%$, 40% and 70%, respectively
849 (Table 2). Comparing these values with those of $T_\infty = 273.15$ K (0°C), it can be noted that a lower ambient temperature
850 leads to a smaller decrease in droplet temperatures and a slight increase in droplet lifetimes in a spatiotemporally
851 evolving environment, for the same RH_∞ , r_0 and P . Fig. 10 and Table 1 depict that for $T_\infty = 263.15$ K (-10°C), the
852 reduction in droplet temperatures is slightly smaller, ~ 21.8 K, 10.7 K, and 4.5 K for environments with $RH_\infty = 10\%$,
853 40%, and 70%, respectively, and droplet lifetimes are longer relative to the higher ambient temperatures of 273.15 K
854 and 268.15 K (Table 2). This is because at a lower ambient temperature, the vapor diffusivity into the ambient air is
855 lower, leading to a weaker evaporation rate with slightly reduced cooling, and extended droplet lifetime, relative to
856 those in an environment with a higher ambient temperature.

857

Deleted: 4

Deleted: From Figs. 9-14, the decrease in droplet temperatures is independent of the initial droplet size if all other initial environmental conditions are kept constant.

Deleted: 10

Deleted: and Fig. 13a-i

Deleted: The nature of these dependencies on r_0 is in good agreement with those reported in Roy et al., (2023).

Deleted: 4

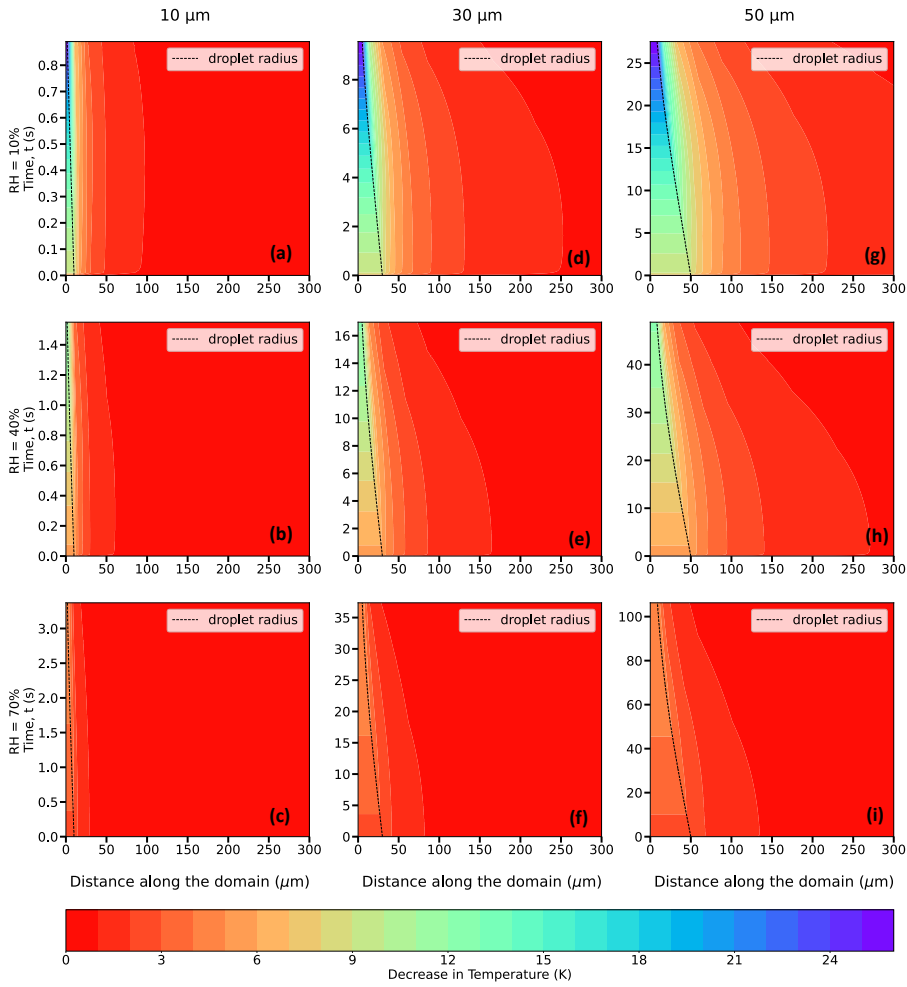
Deleted: 10

Deleted: 1

Deleted: 9

Deleted: , as shown by Roy et al., 2023

Deleted: 1

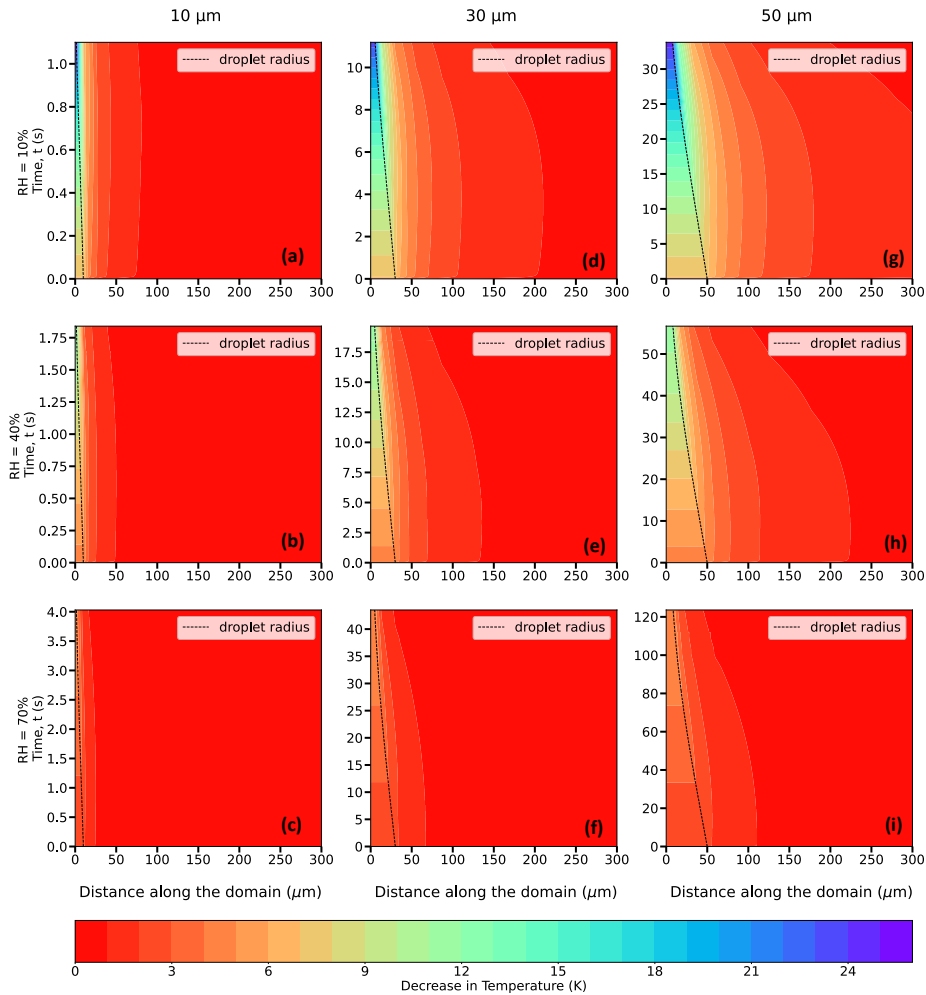


872
 873 **Figure 8: Evolution of the decrease in temperature (in K, shaded contours) from the initial temperature of the domain =**
 874 **273.15 K (0°C), and of the droplet radius (in μm, dashed black trace) for 10 (a,b,c), 30 (d,e,f), and 50 (g,h,i) μm droplets,**
 875 **immersed in an environment with $T_{\infty} = 273.15$ K (0°C), $P = 500$ hPa, and $RH_{\infty} = 10\%$, 40% and 70% .**
 876
 877
 878
 879
 880
 881
 882
 883

T_{∞} (K)	r_0 (μm)	RH_{∞} (%)	$P = 500 \text{ hPa}$					$P = 850 \text{ hPa}$				
			$T_{WB\infty}$ (K)	T_{RRD} (K)	T_i (K)	T_L (K)	$T_{\infty} - T_L$ (K)	$T_{WB\infty}$ (K)	T_{RRD} (K)	T_i (K)	T_L (K)	$T_{\infty} - T_L$ (K)
273.15 (0°C)	10	10	264.94	264.06	264.15	247.15	26	267.20	266.49	266.35	249.03	24.12
		40	267.95	267.41	267.35	261.09	12.06	269.30	268.85	268.95	261.40	11.75
		70	270.67	270.43	270.35	268.21	4.94	271.28	271.07	271.10	268.29	4.86
	30	10	264.94	264.06	264.15	247.33	25.82	267.20	266.49	266.37	249.01	24.14
		40	267.95	267.41	267.35	261.08	12.07	269.30	268.85	268.95	261.43	11.72
		70	270.67	270.43	270.45	268.20	4.95	271.28	271.07	271.15	268.26	4.89
	50	10	264.94	264.06	264.15	247.31	25.84	267.20	266.49	266.37	249.04	24.11
		40	267.95	267.41	267.36	261.09	12.06	269.30	268.85	268.95	261.45	11.7
		70	270.67	270.43	270.45	268.20	4.95	271.28	271.07	271.15	268.29	4.86
268.15 (-5°C)	10	10	261.64	260.90	260.98	244.12	24.03	263.57	263.01	263.15	246.32	21.83
		40	263.96	263.50	263.48	256.77	11.38	265.16	264.79	264.82	257.17	10.98
		70	266.13	265.91	265.9	263.47	4.68	266.68	266.51	266.65	263.57	4.58
	30	10	261.64	260.90	260.85	244.31	23.84	263.57	263.01	263.06	246.18	21.97
		40	263.96	263.50	263.46	256.76	11.39	265.16	264.79	264.69	257.18	10.97
		70	266.13	265.91	265.92	263.47	4.68	266.68	266.51	266.56	263.58	4.57
	50	10	261.64	260.90	260.85	244.29	23.86	263.57	263.01	263.06	246.21	21.94
		40	263.96	263.50	263.47	256.76	11.39	265.16	264.79	264.72	257.16	10.99
		70	266.13	265.91	265.92	263.46	4.69	266.68	266.51	266.56	263.56	4.59
263.15 (-10°C)	10	10	258.14	257.55	257.53	241.38	21.77	259.73	259.28	259.28	243.49	19.66
		40	259.89	259.51	259.65	252.46	10.69	260.90	260.60	260.65	252.97	10.18
		70	261.56	261.38	261.4	258.73	4.42	262.04	261.90	261.90	258.88	4.27
	30	10	258.14	257.55	257.62	241.36	21.79	259.73	259.28	259.28	243.27	19.88
		40	259.89	259.51	259.56	252.47	10.68	260.90	260.60	260.54	252.99	10.16
		70	261.56	261.38	261.39	258.73	4.42	262.04	261.90	261.91	258.88	4.27
	50	10	258.14	257.55	257.62	241.37	21.78	259.73	259.28	259.28	243.48	19.67
		40	259.89	259.51	259.56	252.47	10.68	260.90	260.60	260.56	252.99	10.16
		70	261.56	261.38	261.39	258.73	4.42	262.04	261.90	261.91	258.87	4.28

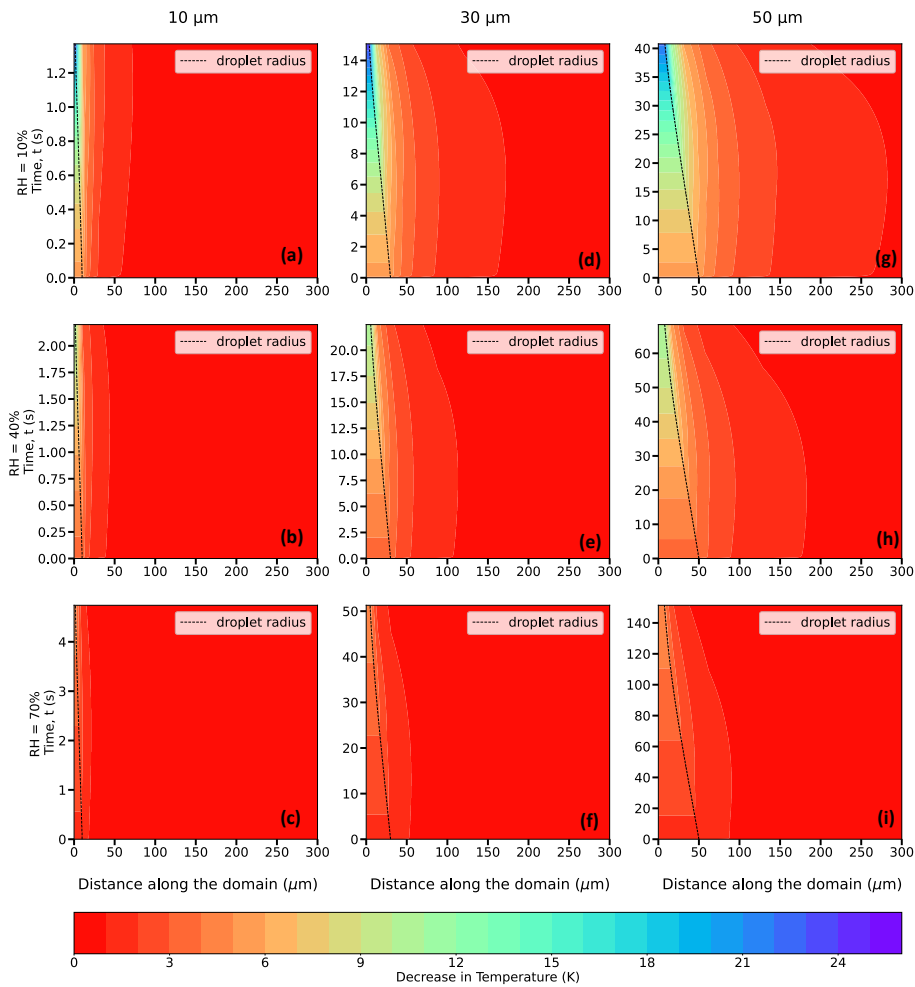
884 Table 1. Comparison between thermodynamic wet bulb temperatures in the environment far away from the droplet
 885 ($T_{WB\infty}$), simulated droplet steady-state temperatures from Roy et al., (2023) (T_{RRD}), slope transition point temperatures
 886 (T_s), and droplet temperatures at the end of their lifetimes from this study (T_L), in K, for initial droplet radii, $r_0 = 10, 30$ and
 887 $50 \mu\text{m}$, relative humidities, $RH_\infty = 10, 40, 70\%$, and pressures, $P = 500$ and 850 hPa, and ambient temperature, $T_\infty = 273.15$
 888 K (0°C), 268.15 K (-5°C) and 263.15 K (-10°C).
 889

Deleted: inflection



890 Figure 9: Same as Fig. 8 but for $T_\infty = 268.15$ K (-5°C).
 891

892



894
895 **Figure 10:** Same as Fig. 8 but for $T_\infty = 263.15$ K (-10°C).

896
897 **4.3.4 Effect of Ambient Pressure, P**

898
899 The spatiotemporal evolution of the temperature and droplet radius of an evaporating droplet were also investigated
900 for a higher ambient pressure, $P = 850$ hPa. For a higher pressure, the corresponding decreases in droplet temperatures
901 are smaller and droplet lifetimes are longer. Under the same environmental conditions but with an increase in ambient
902 pressure, water vapor diffusivity decreases, leading to a decreased evaporation rate, reduced cooling, and extended

- Deleted: 4
- Deleted: Figures. 12-14 depict
- Deleted: t
- Deleted:
- Deleted: similar to the previous figure
- Deleted: s, but now for a
- Deleted: , instead of 500 hPa as shown in Figs. 9-11

droplet lifetimes. For example, for an environment with $T_{\infty} = 273.15$ K (0°C), $P = 850$ hPa, 10, 30 and 50 μm droplets reach 249.0 K, 261.4 K, and 268.3 K for $RH_{\infty} = 10\%$, 40% and 70%, respectively, which are slightly higher as compared to the corresponding droplet temperatures (247.3 K, 261.1 K, and 268.2 K) for $P = 500$ hPa (Table 1). For higher ambient pressures, droplet lifetimes are also increased due to reduced evaporation rate, with 50 μm droplets now surviving for 33.4 s, 55.8 s, and 121.7 s at $P = 850$ hPa, instead of 27.4 s, 48.0 s, 107.5 s for $P = 500$ hPa for $RH_{\infty} = 10\%$, 40% and 70%, respectively (Table 2). Similar trends can also be observed for lower ambient temperatures, 268.15 K and 263.15 K, as shown in Table 2.

Deleted: (Fig. 12 and Table 1)

Deleted: e 1)

Deleted: , and Figs. 10 and 13, and 11

Deleted: and 14.

T_{∞} (K)	r_0 (μm)	RH_{∞} (%)	$P = 500$ hPa				$P = 850$ hPa			
			t_{LC} (s)	t_{RRD} (s)	t_L (s)	$\frac{t_L - t_{LC}}{t_{LC}} \times 100\%$	t_{LC} (s)	t_{RRD} (s)	t_L (s)	$\frac{t_L - t_{LC}}{t_{LC}} \times 100\%$
273.15 (0°C)	10	10	0.26	0.56	0.87	234.62	0.44	0.77	1.11	152.27
		40	0.39	0.89	1.51	287.18	0.66	1.18	1.79	171.21
		70	0.78	1.86	3.36	430.77	1.33	2.43	3.87	190.98
	30	10	2.34	5.02	9.54	307.69	3.98	6.84	11.63	192.21
		40	3.51	7.94	16.68	375.21	5.97	10.59	19.33	223.79
		70	7.03	16.73	37.26	430.01	11.95	21.83	42.30	253.97
	50	10	6.51	13.95	27.43	321.35	11.06	19.06	33.35	201.54
		40	9.76	22.08	48.04	392.21	16.59	29.45	55.78	236.23
		70	19.52	46.46	107.45	450.46	33.18	60.64	121.70	266.79
268.15 (-5°C)	10	10	0.38	0.72	1.05	176.32	0.65	1.01	1.32	103.08
		40	0.58	1.12	1.77	205.17	0.98	1.54	2.15	119.39
		70	1.15	2.31	3.91	240	1.96	3.14	4.60	134.69
	30	10	3.45	6.42	11.40	230.43	5.87	9.03	14.27	143.10
		40	5.18	10.01	19.35	273.55	8.81	13.83	23.32	164.70
		70	10.36	20.81	42.79	313.03	17.61	28.25	50.15	184.78
	50	10	9.59	17.88	32.76	241.61	16.31	25.15	40.99	151.32
		40	14.39	27.86	55.76	287.49	24.46	38.48	67.02	173.99
		70	28.78	57.80	123.10	327.73	48.92	78.48	144.07	194.50
263.15 (-10°C)	10	10	0.57	0.95	1.29	126.34	0.98	1.37	1.68	71.43
		40	0.86	1.45	2.13	147.67	1.47	2.08	2.68	82.31
		70	1.72	2.98	4.60	167.44	2.93	4.21	5.66	93.17

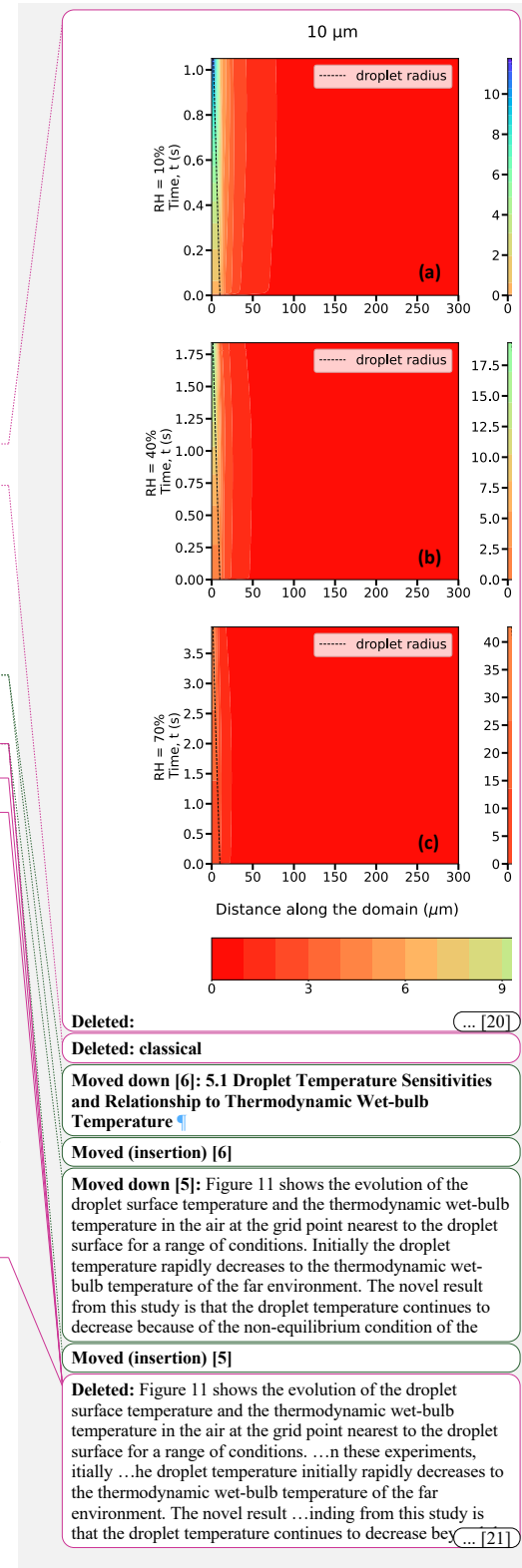
30	10	5.17	8.47	13.95	169.83	8.80	12.28	17.99	104.43
	40	7.76	13.05	23.08	197.42	13.19	18.67	28.83	118.57
	70	15.52	26.79	50.12	222.94	26.39	37.85	61.04	131.29
50	10	14.37	23.59	40.11	179.12	24.43	34.19	51.59	111.17
	40	21.56	36.30	66.42	208.07	36.65	51.93	82.53	125.18
	70	43.12	74.43	144.33	234.72	73.30	105.16	175.50	139.43

Table 2: Comparison between different timescales (in sec) in this and other studies, all for the cut off radii used in this study. These include droplet lifetimes using the Maxwellian diffusion-limited evaporation approach (t_{LC}), the bulk droplet approach in Roy et al., (2023) (t_{RRD}), and as calculated from this study (t_d), for initial droplet radii ($r_0 = 10, 30$ and $50 \mu\text{m}$), relative humidities ($RH_\infty = 10, 40, 70\%$), and pressures ($P = 500$ and 850 hPa), and ambient temperature, $T_\infty = 273.15$ K (0°C), 268.15 K (-5°C) and 263.15 K (-10°C).

5 Discussion

5.1 Droplet Temperature Sensitivities and Relationship to Thermodynamic Wet-bulb Temperature

In these experiments, the droplet temperature initially rapidly decreases to the thermodynamic wet-bulb temperature of the far environment. The novel finding from this study is that the droplet temperature continues to decrease beyond the thermodynamic wet-bulb temperature of the far environment because of the non-equilibrium condition of the thermal and vapor fields during the evaporation process (Fig. 11). The droplet temperature continues to conform to the wet-bulb temperature directly adjacent to the droplet surface, which is lower than the wet-bulb temperature of the far environment. Note that the dependence on T_∞ and P is much smaller than that on RH_∞ . The strong dependence on RH_∞ compared to temperature results from the initial conditions. The droplet temperature initially is in thermal equilibrium with its environment (the droplet has the same temperature as that of the far environment), but the vapor field is far from equilibrium, especially for low relative humidity environments. As a result, the vapor diffusion rate (which depends on the vapor density gradient) far exceeds the thermal diffusion rate (which depends on the temperature gradient). Because the cloud droplets are small, and the relative humidity gradients are large, the droplets never come to an equilibrium state before evaporating completely into the subsaturated air. The water vapor flux into the larger subsaturated environment maintains a vapor density near the droplet surface that approaches but never reaches saturation. As a result, the wet-bulb temperature near the droplet surface continues to fall but at a slower rate that depends on RH_∞ (Fig. 11). The pressure affects both the moisture and temperature diffusion fluxes, so these scale with each other, resulting in pressure not having a strong effect compared to that of the moisture gradient.



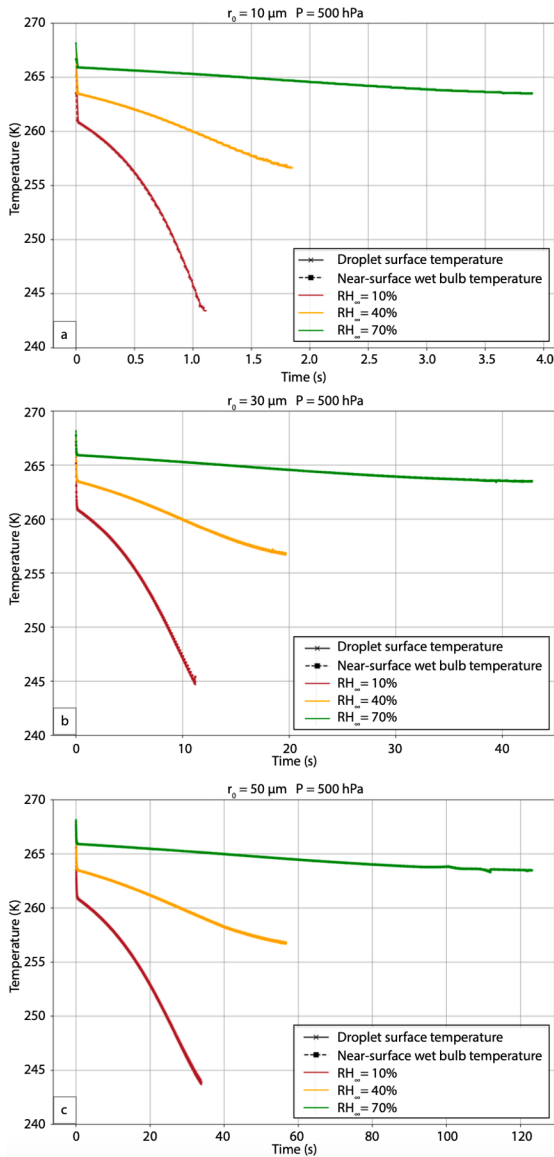


Figure 11: Evolution of droplet surface temperature (in K, solid lines with cross symbols), and near-surface thermodynamic wet-bulb temperature (in K, dashed lines with square symbols) for (a) 10, (b) 30 and (c) 50 μm droplet, immersed in an environment with $T_\infty = 268.15 \text{ K}$ (-5°C), $P = 500 \text{ hPa}$, and three different RH_∞ . The lines representing droplet surface temperature and near-surface thermodynamic wet-bulb temperature essentially overlap.

Moved down [7]: Figure 11: Evolution of droplet surface temperature (in K, solid lines with cross symbols), and near-surface thermodynamic wet-bulb temperature (in K, dashed lines with square symbols) for (a) 10, (b) 30 and (c) 50 μm droplet, immersed in an environment with $T_\infty = 268.15 \text{ K}$ (-5°C), $P = 500 \text{ hPa}$, and three different RH_∞ . The lines representing droplet surface temperature and near-surface thermodynamic wet-bulb temperature essentially overlap.

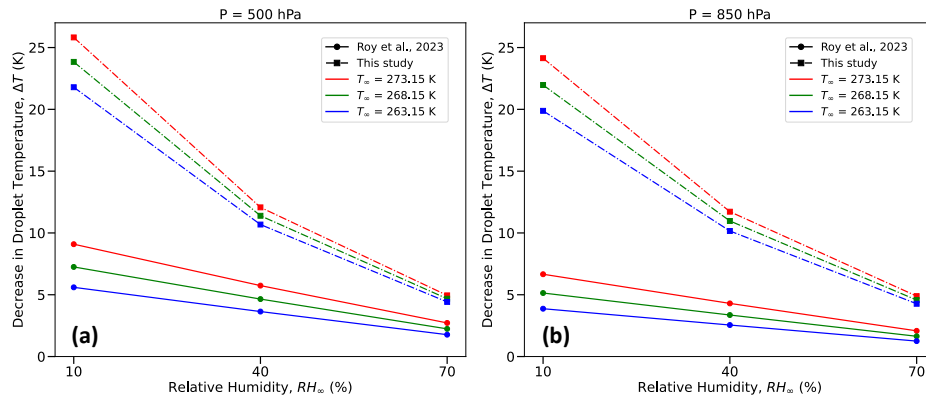
Moved (insertion) [7]

1140
1141
1142
1143
1144
1145

1155
 1156
 1157
 1158
 1159
 1160
 1161
 1162
 1163
 1164
 1165
 1166
 1167
 1168
 1169
 1170
 1171

5.2 Droplet Temperature and Lifetime Comparison with Previous Studies

As noted in the introduction, not many studies in the cloud microphysics literature have taken a close look at the explicit numerical estimation of supercooled, evaporating cloud droplet temperatures for a wide range of environmental conditions. Previously, a study by Srivastava and Coen (1992) investigated the evaporation of isolated, stationary droplets by iteratively solving the steady-state solutions, using saturation vapor pressure relations from Wexler (1976) to calculate saturation vapor density, and assumed the heat storage terms in the droplet heat budget to be negligible. Roy et al., (2023), solving for time-dependent heat and mass transfer between single, stationary cloud droplets evaporating in infinitely large, prescribed ambient environments, demonstrated that the temperatures of the cloud droplets reach steady-state quite quickly (< 0.3 s). Their steady-state droplet temperatures agreed well with those of Srivastava and Coen (1992) and could be approximated by the thermodynamic wet-bulb temperature of the ambient environment. The current study advances the idealized framework of droplet evaporation as described in Roy et al., (2023) by including the impact of internal heat gradients within the droplet and resolving the spatiotemporally evolving thermal and vapor density gradients between the droplet and its immediate environment to estimate the evaporating droplet temperature and lifetime with higher accuracy.



1172
 1173
 1174
 1175
 1176
 1177
 1178
 1179
 1180
 1181

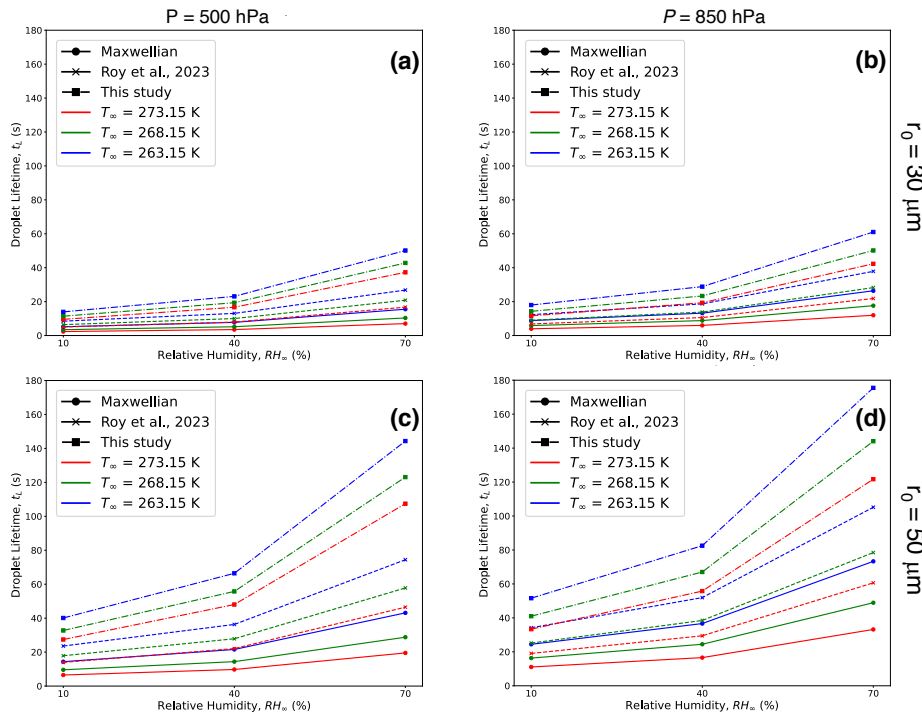
Figure 12: Comparison between the decrease in droplet temperatures (in K) from an initial temperature the same as T_∞ , calculated using the bulk droplet model from Roy et al., (2023) (dashed lines), and this study (dashed-dotted lines), for initial droplet radii, $r_0 = 10, 30$ or $50 \mu\text{m}$, relative humidities ($RH_\infty = 10, 40, 70 \%$), and pressures, $P = 500 \text{ hPa}$ (left column), and 850 hPa right column), and $T_\infty = 273.15 \text{ K}$ (0°C , red), 268.15 K (-5°C , green) and 263.15 K (-10°C , blue).

Table 1 provides a comparison between thermodynamic wet bulb temperatures of the initial environment ($T_{WB\infty}$), simulated droplet steady-state temperatures from Roy et al. (2023) (T_{RRD}), and droplet temperatures at the end of their lifetimes from this study (T_L), in K for several environments. Interestingly, the temperatures at the slope transition point, T_i , as defined in Sec. 3e, are in excellent agreement with $T_{WB\infty}$ and T_{RRD} . In the current study, the droplet temperature continues to decrease almost steadily as the immediate environment in the vicinity of the droplet cools,

Deleted: S
 Deleted: Roy et al., (2023)
 Deleted: 5
 Deleted: In order to model a more realistic scenario of an isolated droplet evaporating in a subsaturated environment
 Deleted: , t

Deleted: inflection

1189 finally reaching T_L , unlike the evaporating droplet achieving a steady-state temperature in a prescribed ambient
 1190 environment far away from the droplet in Roy et al., (2023). The evaporating droplet temperature essentially keeps
 1191 adjusting to the thermodynamic wet-bulb temperature of its immediate changing environment. Therefore, the more
 1192 realistic simulations of evaporating cloud droplets that include the effect of spatiotemporally varying ambient air
 1193 thermal and vapor density gradients, as shown in this study, reveal that droplets can potentially achieve even lower
 1194 temperatures than previously known or estimated from past studies (Srivastava and Coen, 1992; Roy et al., 2023). The
 1195 decrease in droplet temperatures from their initial temperatures can be much larger, especially for drier environments,
 1196 as much as 25.8 K for $RH_\infty = 10\%$ and 5.0 K for $RH_\infty = 70\%$, for an environment with $P = 500$ hPa, and $T_\infty = 273.15$
 1197 K (Table 1 and Fig. 12a). As shown in Fig. 12, the magnitude of reduction in droplet temperatures decreases with
 1198 higher ambient RH_∞ and P , and lower T_∞ , similar to previous studies (Srivastava and Coen, 1992; Roy et al., 2023).



1200 **Figure 13: Comparison between droplet lifetimes (as defined in this study) calculated using the Maxwellian diffusion-limited**
 1201 **evaporation approach (solid lines), bulk droplet model from Roy et al., (2023) (dashed lines), and this study (dashed-dotted**
 1202 **lines), for initial droplet radii, $r_0 = 30 \mu\text{m}$ (upper panel), and $50 \mu\text{m}$ (lower panel), relative humidities ($RH_\infty = 10, 40, 70\%$),**
 1203 **and pressures, $P = 500$ hPa (left column), and 850 hPa (right column), and ambient temperature, $T_\infty = 273.15$ K (0°C , red),**
 1204 **268.15 K (-5°C , green) and 263.15 K (-10°C , blue). $10 \mu\text{m}$ droplets (not shown here) have much smaller lifetimes compared**
 1205 **to 30 and $50 \mu\text{m}$ droplets.**

1206 Table 2 and Fig. 13 provide comparisons between $10, 30$ and $50 \mu\text{m}$ droplet lifetimes (as defined earlier in Sec. 3a)
 1207 using the Maxwellian pure-diffusion-limited evaporation approach (t_{LC}), which ignores evaporative cooling at the

Deleted: 5

Deleted: 5

Deleted: classical

Deleted: 6

Deleted: classical

1213 droplet surface (Maxwell, 1890; Eq 13-10 of Pruppacher and Klett, 1997), the “bulk” droplet approach as described
 1214 in Roy et al., (2023) (t_{RRD}), which ignores internal droplet heat transfer and spatiotemporally varying thermal and
 1215 moisture gradients in the ambient air, and results from this study (t_L). The magnitude of t_L is greater than the
 1216 corresponding values of t_{LC} and t_{RRD} . This is because the droplet temperatures in this study never reach steady-state,
 1217 and are much lower than the corresponding droplet temperatures from the diffusion-limited approach ($\sim T_\infty$), and Roy
 1218 et al., (2023) ($\sim T_{RRD}$). The greater decrease in evaporating droplet temperature leads to a greater reduction in saturation
 1219 vapor pressure at the droplet surface. This results in a slower droplet evaporation rate, therefore increasing the droplet
 1220 lifetime. As shown in Fig. 13, the increase in droplet lifetime depends on the environmental subsaturation, ambient
 1221 temperatures, and pressures, with a greater increase for more humid, higher pressure, and lower ambient temperature
 1222 environments. The increase in droplet lifetimes can potentially enhance ice nucleation by increasing the chances of
 1223 activation of ice nucleating particles (INPs) within the supercooled cloud droplets (see Sect. 5.3).

1225 5.3 Implications for ice nucleation

1226
 1227 Ice nucleation rates are influenced by temperature (Wright and Petters, 2013; Kanji et al., 2017) and time (Vali, 1994).
 1228 There are two theories in ice nucleation modeling: the time-independent "singular hypothesis," which suggests
 1229 instantaneous ice formation, and the time-dependent "stochastic hypothesis," which proposes that ice clusters in
 1230 embryos form and vanish continually, with a frequency that depends on temperature. Supercooled cloud droplet
 1231 temperatures and their lifetimes are potential contributing factors for the enhancement of ice formation within
 1232 evaporating regions of clouds such as cloud-tops and edges. As discussed in Roy et al., (2023), evaporative cooling
 1233 of supercooled cloud droplets in subsaturated environments can enhance ice nucleation near cloud boundaries in two
 1234 ways: by instantly increasing ice-nucleating particle activation due to lower droplet temperatures (consistent with the
 1235 singular hypothesis) and/or by extending supercooled droplet lifetimes, allowing more time for nucleation events
 1236 (consistent with the stochastic hypothesis). Based on limited laboratory investigations available on time dependency
 1237 of heterogeneous ice nucleation, conducted between temperatures -14 and -30 °C, varying fractions of the droplets
 1238 were reported to freeze within a range of 1 s to 500 s (Welti et al., 2012; Broadley et al., 2012; Murray et al., 2012;
 1239 Jakobsson et al., 2022).

1241 Droplet freezing events can potentially occur within the time frame when the evaporating cloud droplets reach lower
 1242 temperatures due to evaporative cooling before they completely dissipate into the subsaturated air. This can be seen
 1243 by comparing the values in Table 2 and Fig. 13 with reported droplet freezing timescales available from experimental
 1244 studies. Droplet lifetimes as estimated from both approaches (t_{RRD} and t_L), which include droplet evaporative cooling,
 1245 are longer as compared to the Maxwellian diffusion-limited evaporation approach (t_{LC}), allowing more time for
 1246 potential occurrence of an ice nucleation event. For temperatures between -5 °C and -10 °C, for the three different
 1247 subsaturated environments ($RH_\infty = 10, 40, \text{ and } 70\%$) examined in this analysis, t_{RRD} typically ranged from 0.7 - 4.2 s
 1248 for 10 μm , 6-38 s for 30 μm and 18-105 s for 50 μm initial radius of droplets, respectively. For similar environments,
 1249 $t_L > t_{RRD} > t_{LC}$, with t_L typically ranging from 1.1-5.7 s for 10 μm , 11-61 s for 30 μm and 33-176 s for 50 μm initial

Deleted:

Deleted: This can be explained by

Deleted: t

Deleted: ing

Deleted: 6

Deleted: is

Deleted: is

Deleted: ion

Deleted: b

Moved (insertion) [4]

Deleted: Comparing these values with reported droplet freezing timescales available from experimental studies,

Deleted: d

Deleted: se

Deleted: can

Formatted: Indent: First line: 0"

Deleted: As shown in Table 2 and Fig. 16,

Deleted: d

Deleted: classical

1267 radii droplets, respectively. For larger droplets, say 30 and 50 μm , the droplets survive much longer as compared to
1268 10 μm droplets, likely enhancing the chances of an ice nucleation event.

1269
1270 Results from this study further strengthen evidence of the hypothesized mechanism of enhancement of ice nucleation
1271 via droplet evaporation. Together with the consistent observation of supercooled water in cloud-top generating cells
1272 (Plummer et al., 2014; Zaremba et al., 2024), these results contribute to explaining the observations of the prodigious
1273 production of ice particles produced in generating cells at the cloud-tops of winter storms [and other clouds](#) (e.g.,
1274 Plummer et al., 2015, [Wang et al., 2020](#)), [Rauber et al. \(1986\)](#), [Plummer et al. \(2015\)](#), and [Tessendorf et al. \(2024\)](#)
1275 have shown that cloud droplet concentrations at the generating cell level near cloud-tops are of the order of 30-50 cm^{-3} ,
1276 while ice-particle concentrations in the plumes of ice particles falling beneath generating cells are of the order of
1277 0.01 cm^{-3} . Based on these values, if less than one frozen cloud droplet in 1000 survive sublimation after freezing and
1278 fall back into the cloud, that would be sufficient to create the ice-particles observed falling from a generating cell.

1279
1280 Due to the observational evidence of a higher dependency of ice nucleation on temperature than time (Wright and
1281 Petters, 2013), and the increased difficulty of representing time-dependent stochastic nucleation in numerical models,
1282 the simpler and more widely used approach is to use the time-dependent singular hypothesis framework to simulate
1283 ice initiation processes. Drawing from theoretical insights, laboratory experiments, and field campaigns, numerous
1284 parameterization methods for modeling heterogeneous ice nucleation in cloud and climate models have been created
1285 over the years (Fletcher, 1962; Cooper, 1986; Meyers et al., 1992; DeMott et al., 1998; Khvorostyanov and Curry,
1286 2000; Phillips et al., 2008). Most of the conventionally used schemes (Fletcher, 1962; Cooper, 1986; Demott et al.,
1287 2010) share a common feature, which is the utilization of the ambient air temperature for estimating activated INPs,
1288 as opposed to relying on the droplet temperature, even for primary ice-nucleation modes such as immersion freezing
1289 and contact nucleation.

1290
1291 Similar to Roy et al. (2023), we investigate the maximum enhancement in activated INP concentrations that can occur
1292 due to evaporative cooling of supercooled water droplets in a spatiotemporally varying environment, assuming that
1293 the activation in the parameterization schemes (Fletcher, 1962; Cooper, 1986; Demott et al., 2010) is related to the
1294 droplet temperatures towards the end of their lifetimes (T_L) rather than the ambient temperature. Fig. 14 presents a
1295 comparison between Roy et al. (2023), and the current study in terms of the highest fractional increase in activated
1296 ice-nucleating particles (INPs), as projected through the Fletcher, Cooper, and Demott schemes (considering ambient
1297 aerosol concentration, N_a , with diameters greater than 0.5 μm). Owing to even lower droplet temperatures during
1298 evaporation, the fractional increase in activated INPs is higher as calculated from this study, with several orders of
1299 magnitude increase for drier environments. For example, the Fletcher Scheme predicts an enhancement in activated
1300 INPs by a factor of $\sim 10^6$ for $RH_\infty = 10\%$, $T_\infty = 268.15 \text{ K}$, $P = 500 \text{ hPa}$ based on droplet temperatures from this study,
1301 while the corresponding number from Roy et al. (2023) is ~ 100 (Fig. 14a). The fractional increases are slightly smaller
1302 for higher pressure environments due to lower evaporative cooling of the droplets under such conditions (compare
1303 Figs. 14a, d, b, e, and c, f). Consistent with previous results from Roy et al. (2023), compared to the Fletcher Scheme,

Moved up [4]: Comparing these values with reported droplet freezing timescales available from experimental studies, droplet freezing events can potentially occur within the time frame when these droplets can reach lower temperatures due to evaporative cooling before they completely dissipate into the subsaturated air.

Deleted: 7

Deleted: 7

Deleted: 7

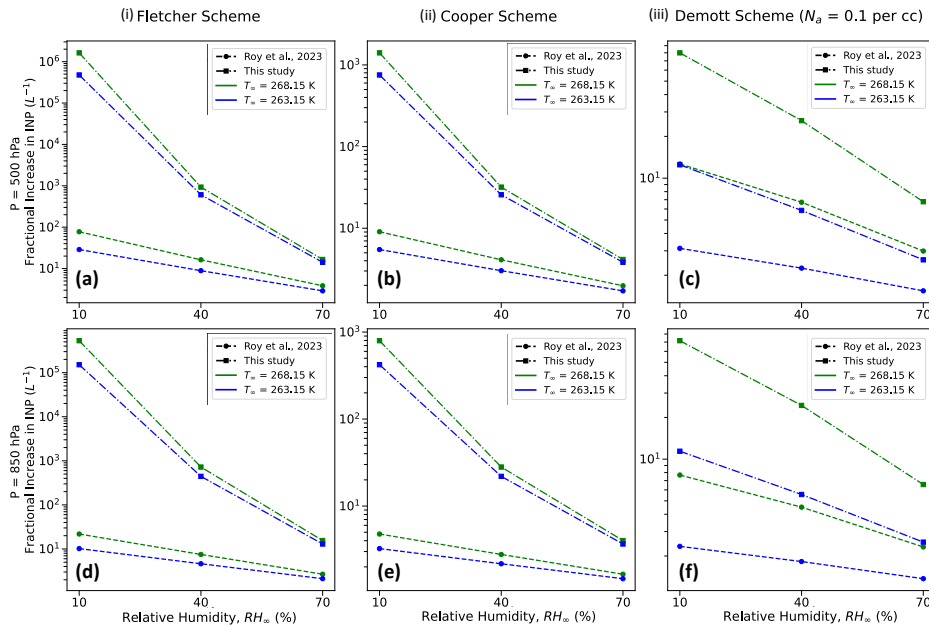
1313 the Cooper and Demott schemes demonstrate relatively lower enhancement in activated INPs. For the same
 1314 environment stated earlier, the corresponding activated INP enhancement factor values for Cooper and Demott
 1315 schemes are $\sim 10^3$ and 80, respectively (Figs. 14b and c).

1317 Therefore, results from the current study further corroborate the hypothesized ice nucleation enhancement mechanism
 1318 through evaporative cooling of supercooled droplets (Mossop et al., 1968; Young, 1974; Beard, 1992; Roy et al.,
 1319 2023), providing much higher estimates of activated INP concentrations from previous analyses (Roy et al., 2023).
 1320 This potential increase in INP concentrations in subsaturated environments near cloud tops and edges, particularly at
 1321 higher sub-freezing temperatures, may partially help resolve the several orders of magnitude discrepancy between
 1322 predicted INP and observed ice particle concentrations in such regions of the cloud. To evaluate the effectiveness of
 1323 the potential ice-nucleation enhancement mechanism through evaporation, future modeling experiments within a
 1324 robust dynamical model setup, considering a population of both freezing and evaporating droplets, along with their
 1325 lifetimes, droplet-droplet interaction, different species of INPs, and the impact of turbulence and other feedbacks, are
 1326 required.

Deleted: 7

Formatted: Border: Top: (No border), Bottom: (No border), Left: (No border), Right: (No border), Between : (No border)

Deleted: ¶



1327
 1328 **Figure 14: Comparison between the maximum fractional increase in INPs as estimated by Roy et al., (2023) and this study**
 1329 **for three different parameterization schemes: (i) Fletcher (1962) (ii) Cooper (1986), and (iii) Demott et al., (2010), for three**
 1330 **different environmental relative humidities ($RH_{\infty} = 10, 40$ and 70%), and two ambient temperatures ($T_{\infty} = 268.15$ K (-5° C)**
 1331 **and 263.15 K (-10° C) and two different pressures ($P = 500$ and 850 hPa).**

1332
 1333 **6 Conclusions**

1336

1337 In this study, we presented a quantitative investigation of the temperature and lifetime of an evaporating droplet,
1338 considering internal thermal gradients within the droplet as well as resolving spatiotemporally varying thermal and
1339 vapor density gradients in the surrounding ambient air. The computational approach involved solving the Navier-
1340 Stokes and continuity equations, coupled with heat and vapor diffusion equations, using an advanced numerical model
1341 that employs the finite element method. This is the first simulation of the spatiotemporal evolution of droplet
1342 temperature, radius, and its environment for an isolated, stationary, and supercooled cloud droplet evaporating in
1343 various subsaturated environmental conditions. Various ambient pressure (P), temperature (T_a), relative humidity
1344 (RH_a), and initial droplet radii (r_0) were considered. The motivation behind this study was to provide more exacting
1345 calculations to support the hypothesized ice nucleation enhancement mechanism due to the evaporation of supercooled
1346 cloud droplets at cloud boundaries, such as cloud-top ice-generating cells, and for ambient temperatures between 0°C
1347 and -10°C where ice nucleation is least effective.

1348

1349 The numerical simulations show for typical cloud droplet sizes ($r_0 = 10, 30, 50 \mu\text{m}$) and environmental conditions
1350 considered here, the internal thermal gradients dissipate quite quickly ($\leq 0.3 \text{ s}$) when the droplet is introduced to a new
1351 subsaturated environment. Thus, spatial thermal gradients within the droplet can be reasonably ignored. Hence, one
1352 can potentially ignore the extra computational expense of simulating conductive heat transfer within the droplet for
1353 timescales $> 1 \text{ s}$.

1354

1355 The results from this study are similar to findings from the literature that an evaporating supercooled cloud droplet
1356 can exist at a temperature lower than that of the ambient atmosphere and that the tendencies of the dependence of
1357 decrease in droplet temperatures on environmental factors and initial droplet sizes (Srivastava and Coen, 1992; Roy
1358 et. al, 2023). The novelty of this study lies in demonstrating that the magnitude of droplet cooling can be much higher
1359 than estimated from past studies of droplet evaporation, especially for drier environments. For example, a droplet
1360 evaporating in an environment with $P = 500 \text{ hPa}$, $T_a = 268.15 \text{ K}$ (-5°C), $RH_a = 10\%$, Roy et al., (2023) estimated a
1361 7.3 K decrease in droplet temperature, while this study shows that there can be as much as a 23.8 K decrease in droplet
1362 temperature. This is because previous studies assumed prescribed ambient environments at all distances from the
1363 droplet, while this analysis shows that as a droplet evaporates and cools, the air in the vicinity of the droplet cools as
1364 well, giving rise to spatiotemporally varying thermal and vapor density fields in the immediate environment
1365 surrounding the droplet. Here, the net conductive warming from the environmental air enveloping the droplet is lower
1366 as compared to Roy et al., (2023), effectively leading to a much lower droplet temperature. At a particular time, the
1367 strength and radial dependence of these gradients depend on the subsaturation of the air medium and the magnitude
1368 of droplet cooling due to evaporation, with the largest cooling at lower RH_a . In this study, the temperature and vapor
1369 density in the ambient air continually evolve, thus affecting the transfer of heat and vapor between the droplet surface
1370 and the environment far away from the droplet. This affects the temperature evolution and decay rates of the
1371 evaporating droplet to a greater degree than shown in previous studies for a similar environment (Srivastava and
1372 Cohen, 1992; Roy et al. 2023).

Deleted: Since evaporation is a surface phenomenon, there is a legitimate interest in computing droplet internal thermal gradients and investigating if the droplet surface gets preferentially cooled during droplet evaporation, with regards to the activation of ice nucleating particles.

Deleted: support

Deleted: corroborate

Deleted: Decreases in droplet temperatures are smaller for higher ambient RH_a and P , and lower T_a , qualitatively in accordance with previous studies (Srivastava and Coen, 1992; Roy et al., 2023).

1384
1385 This study also demonstrated that the lifetimes of the evaporating droplets are longer compared to Roy et al. (2023)
1386 because as the droplet temperature gets lower, the saturation vapor pressure at the droplet surface reduces, leading to
1387 a weaker evaporation rate. For an environment with $P = 500$ hPa, $T_{\infty} = 268.15$ K (-5°C), $RH_{\infty} = 10\%$, a 50 μm droplet
1388 reaches the end of its lifetime, as defined in this study, in 32.8s , while the corresponding values for the diffusion-
1389 limited evaporation approach as estimated from Roy et. al, (2023) are 9.6 s and 17.9 s, respectively. The rates of
1390 evaporation tend to be lower in this study due to even lower droplet temperatures as well as spatiotemporally varying
1391 vapor density gradients around the droplets. As the droplet evaporates, the envelope of air surrounding the droplet is
1392 colder, has lower values of diffusivity leading to lower evaporation rates, and has higher vapor concentration than the
1393 ambient air, thus decreasing the evaporation rates.

1394
1395 To summarize, if one considers the more realistic case of droplet evaporation, including the spatiotemporally varying
1396 thermal and vapor density gradients in the vicinity of the water droplet, the evaporating droplet can experience a
1397 substantial reduction in temperatures by several degrees, strongly dependent on the ambient relative humidity and
1398 weakly dependent on ambient pressure and temperature. Similar to the case of an isolated, stationary droplet
1399 evaporating in a prescribed ambient environment, the droplet almost immediately reaches its slope transition point
1400 temperature, which can be well-approximated by the thermodynamic wet-bulb temperature of the initial ambient
1401 environment around the droplet. Droplet temperatures then continue to steadily decrease as they adjust to the evolving
1402 thermodynamic wet-bulb temperature of the surrounding air. In more humid environments, the droplets may not
1403 experience a larger droplet cooling, but their lifetimes, as defined in this study, get extended by tens of seconds as
1404 compared to the Maxwellian estimation which neglects droplet cooling.

Deleted: tens of

Deleted: inflection point

Deleted: However, unlike the former case, the

Deleted: d

Deleted: in this study

Deleted: classical

1406 The current analysis also demonstrates that lower evaporating droplet temperatures would lead to an enhancement of
1407 activated INPs from three widely used INP parameterization schemes, further corroborating the hypothesized ice
1408 nucleation enhancement mechanism through evaporative cooling of supercooled droplets. Notably, the estimates of
1409 activated INP concentrations from this study are higher than previous analyses, as the droplet temperatures are much
1410 lower towards the end of their lifetimes, with several orders of magnitude increase in activated INPs for drier
1411 environments. The Fletcher Scheme predicts the greatest enhancement in activated INPs by a factor of $\sim 10^6$ for RH_{∞}
1412 $= 10\%$, $T_{\infty} = 268.15$ K, $P = 500$ hPa, while the corresponding enhancement factor values for Cooper and Demott
1413 schemes are $\sim 10^3$ and 80 , respectively.

1414
1415 This study suggests a need for a more in-depth examination of supercooled cloud droplet temperatures and their
1416 lifetimes in subsaturated environments, especially when simulating heterogeneous ice nucleation processes that
1417 require the presence of supercooled water droplets. This is crucial because the concentration of activated ice-
1418 nucleating particles (INPs) is influenced by both droplet temperature and how long evaporating droplets persist.
1419 Additionally, the findings from this investigation may also partially help understand disparities between observed ice
1420 particle concentrations and activated INPs, especially at relatively higher sub- 0°C temperatures. Including the effect

1427 of droplet evaporative cooling on droplet temperatures and lifetimes, while modeling cloud microphysical processes
1428 in subsaturated environments, will also lead to improved accuracy of the evolution of the droplet size distribution as
1429 well as primary ice nucleation mechanisms.

1430
1431 **Author contribution:** PR, RMR and LDG conceptualized the problem and numerical experiments. PR designed and
1432 performed the simulations, analyzed the data, and prepared the first draft of the manuscript. RMR and LDG reviewed
1433 and edited the manuscript. RMR and LDG acquired required funding for the project.

1434

1435 **Competing interests:** The authors have no competing interests.

1436

1437 **Acknowledgements:** This work was funded by the NASA CAMP²Ex program under grant 80NSSC18K0144 and the
1438 NASA Earth Venture Suborbital-3 (EVS-3) IMPACTS program under grant 80NSSC19K0355. This research was
1439 also supported by the National Science Foundation under grant NSF AGS-2016106.

1440

1441 **Code/Data availability:** This modeling analysis used the proprietary COMSOL Multiphysics version 6.0 software
1442 package which can be licensed through <https://www.comsol.com/>.

1443

1444 **References**

1445

1446 Alduchov, O.A. and Eskridge, R.E.: Improved Magnus form approximation of saturation vapor pressure, *Journal of*
1447 *Applied Meteorology and Climatology*, 35(4), pp.601-609, [https://doi.org/10.1175/1520-](https://doi.org/10.1175/1520-0450(1996)035<0601:IMFAOS>2.0.CO;2)
1448 [0450\(1996\)035<0601:IMFAOS>2.0.CO;2](https://doi.org/10.1175/1520-0450(1996)035<0601:IMFAOS>2.0.CO;2), 1996.

1449 [American Meteorological Society \(AMS 2024\): Generating cell. https://glossary.ametsoc.org/wiki/Generating_cell](https://glossary.ametsoc.org/wiki/Generating_cell)
1450 [\(Last accessed May 10, 2024\)](https://glossary.ametsoc.org/wiki/Generating_cell)

1451 Beard, K.: Ice Initiation in warm-base convective clouds: An assessment of microphysical mechanisms, *Atmos. Res.*,
1452 28, 125-152, [https://doi.org/10.1016/0169-8095\(92\)90024-5](https://doi.org/10.1016/0169-8095(92)90024-5), 1992.

1453 [Biddle, J.W., Holten, V., Sengers, J.V. and Anisimov, M.A.: Thermal conductivity of supercooled water. *Physical*
1454 *Review E*, 87\(4\), p.042302, <https://doi.org/10.1103/PhysRevE.87.042302>, 2013.](https://doi.org/10.1103/PhysRevE.87.042302)

1455 Broadley, S.L., Murray, B.J., Herbert, R.J., Atkinson, J.D., Dobbie, S., Malkin, T.L., Condliffe, E. and Neve, L.:
1456 Immersion mode heterogeneous ice nucleation by an illite rich powder representative of atmospheric mineral
1457 dust, *Atmospheric Chemistry and Physics*, 12(1), pp.287-307, <https://doi.org/10.5194/acp-12-287-2012>,
1458 2012.

1459 Chushak, Y.G. and Bartell, L.S.: Simulations of spontaneous phase transitions in large, deeply supercooled clusters
1460 of SeF₆, *The Journal of Physical Chemistry B*, 103(50), pp.11196-11204, <https://doi.org/10.1021/jp992818g>,
1461 1999.

1462 Chushak, Y. and Bartell, L.S.: Crystal nucleation and growth in large clusters of SeF₆ from molecular dynamics
1463 simulations, *The Journal of Physical Chemistry A*, 104(41), pp.9328-9336,
1464 <https://doi.org/10.1021/jp002107e>, 2000.

1465 COMSOL 2023a Cylindrical System Documentation, Last Accessed Sept 15, 2023
1466 https://doc.comsol.com/5.5/doc/com.comsol.help.comsol/comsol_ref_definitions.12.090.html
1467 COMSOL 2023b Infinite Element Domain Documentation, Last Accessed Sept 15, 2023
1468 https://doc.comsol.com/5.5/doc/com.comsol.help.comsol/comsol_ref_definitions.12.116.html
1469 COMSOL 2023c Free Triangular Documentation, Last Accessed Sept 15, 2023
1470 https://doc.comsol.com/5.5/doc/com.comsol.help.comsol/comsol_ref_mesh.15.38.html
1471 COMSOL 2023d Mapped Documentation, Last Accessed Sept 15, 2023
1472 https://doc.comsol.com/5.6/doc/com.comsol.help.comsol/comsol_ref_mesh.20.40.html
1473 Cooper, W.A.: Ice initiation in natural clouds. In Precipitation enhancement—A scientific challenge (pp. 29-32).
1474 American Meteorological Society, Boston, MA, <https://doi.org/10.1175/0065-9401-21.43.29>, 1986.
1475 DeMott, P.J., Rogers, D.C., Kreidenweis, S.M., Chen, Y., Twohy, C.H., Baumgardner, D., Heymsfield, A.J. and Chan,
1476 K.R.: The role of heterogeneous freezing nucleation in upper tropospheric clouds: Inferences from
1477 SUCCESS, *Geophysical Research Letters*, 25(9), pp.1387-1390, <https://doi.org/10.1029/97GL03779>, 1998.
1478 DeMott, P.J., Prenni, A.J., Liu, X., Kreidenweis, S.M., Petters, M.D., Twohy, C.H., Richardson, M.S., Eidhammer,
1479 T. and Rogers, D.: Predicting global atmospheric ice nuclei distributions and their impacts on
1480 climate, *Proceedings of the National Academy of Sciences*, 107(25), pp.11217-11222,
1481 <https://doi.org/10.1073/pnas.0910818107>, 2010.
1482 Djikaev, Y.S., Tabazadeh, A., Hamill, P. and Reiss, H.: Thermodynamic conditions for the surface-stimulated
1483 crystallization of atmospheric droplets, *The Journal of Physical Chemistry A*, 106(43), pp.10247-10253,
1484 <https://doi.org/10.1021/jp021044s>, 2002.
1485 Djikaev, Y.S. and Ruckenstein, E.: Thermodynamics of heterogeneous crystal nucleation in contact and immersion
1486 modes, *The Journal of Physical Chemistry A*, 112(46), pp.11677-11687, <https://doi.org/10.1021/jp803155f>,
1487 2008.
1488 Fletcher, N.H.: The physics of rainclouds/NH Fletcher; with an introductory chapter by P. Squires and a foreword by
1489 EG Bowen. Cambridge University Press, <https://doi.org/10.1002/qj.49708837821>, 1962.
1490 Fukuta, N.: Theories of competitive cloud droplet growth and their application to cloud physics studies, *Journal of*
1491 *the Atmospheric Sciences*, 49, 1107-1114, [https://doi.org/10.1175/1520-](https://doi.org/10.1175/1520-0469(1992)049<1107:TOCCDG>2.0.CO;2)
1492 [0469\(1992\)049<1107:TOCCDG>2.0.CO;2](https://doi.org/10.1175/1520-0469(1992)049<1107:TOCCDG>2.0.CO;2), 1992.
1493 Grabowski, W.W. and Wang, L.P.: Growth of cloud droplets in a turbulent environment, *Annual Review of Fluid*
1494 *Mechanics*, 45, pp.293-324, <https://doi.org/10.1146/annurev-fluid-011212-140750>, 2013.
1495 Hall, W.D. and Pruppacher, H.R.: The survival of ice particles falling from cirrus clouds in subsaturated air, *Journal*
1496 *of Atmospheric Sciences*, 33(10), pp.1995-2006, [https://doi.org/10.1175/1520-](https://doi.org/10.1175/1520-0469(1976)033<1995:TSOIPF>2.0.CO;2)
1497 [0469\(1976\)033<1995:TSOIPF>2.0.CO;2](https://doi.org/10.1175/1520-0469(1976)033<1995:TSOIPF>2.0.CO;2), 1976.
1498 Jakobsson, J.K., Waman, D.B., Phillips, V.T. and Bjerring Kristensen, T.: Time dependence of heterogeneous ice
1499 nucleation by ambient aerosols: laboratory observations and a formulation for models. *Atmospheric*
1500 *Chemistry and Physics*, 22(10), pp.6717-6748, <https://doi.org/10.5194/acp-22-6717-2022>, 2022.

1501 Kanji, Z. A., Ladino, L. A., Wex H., Boose, Y., Burkert-Kohn, M., Cziczo, D. J. and Krämer, M.: Overview of Ice
1502 Nucleating Particles, *Meteor. Monogr.*, **58**, 1.1–1.33, [https://doi.org/10.1175/AMSMONOGRAPHS-D-16-](https://doi.org/10.1175/AMSMONOGRAPHS-D-16-0006.1)
1503 [0006.1](https://doi.org/10.1175/AMSMONOGRAPHS-D-16-0006.1), 2017.

1504 Khain, A.P. and Pinsky, M.: Physical processes in clouds and cloud modeling, Cambridge University Press, 2018.

1505 Khvorostyanov, V.I. and Curry, J.A.: A new theory of heterogeneous ice nucleation for application in cloud and
1506 climate models, *Geophysical Research Letters*, **27**(24), pp.4081-4084,
1507 <https://doi.org/10.1029/1999GL011211>, 2000.

1508 Khvorostyanov, V. and Sassen, K.: Toward the theory of homogeneous nucleation and its parameterization for cloud
1509 models, *Geophysical research letters*, **25**(16), pp.3155-3158, <https://doi.org/10.1029/98GL02332>, 1998.

1510 Kinzer, G. D., and Gunn, R.: The evaporation, temperature and thermal relaxation-time of freely falling waterdrops,
1511 *J. Meteor.*, **8**, 71–83. [https://doi.org/10.1175/1520-0469\(1951\)008<0071:TETATR>2.0.CO;2](https://doi.org/10.1175/1520-0469(1951)008<0071:TETATR>2.0.CO;2), 1951.

1512 Lü, Y.J., Xie, W.J. and Wei, B.: Observation of ice nucleation in acoustically levitated water drops, *Applied Physics*
1513 *Letters*, **87**(18), <http://dx.doi.org/10.1063/1.2126801>, 2005.

1514 Marquis, J. and Harrington, J.Y.: Radiative influences on drop and cloud condensation nuclei equilibrium in
1515 stratocumulus, *Journal of Geophysical Research: Atmospheres*, **110**(D10),
1516 <https://doi.org/10.1029/2004JD005401>, 2005.

1517 Maxwell, J.C.: Theory of the wet bulb thermometer, *Scientific Papers of James Clerk Maxwell*, **2**, p.636, 1890.

1518 Meyers, M.P., DeMott, P.J. and Cotton, W.R.: New primary ice-nucleation parameterizations in an explicit cloud
1519 model, *Journal of Applied Meteorology and Climatology*, **31**(7), pp.708-721, [https://doi.org/10.1175/1520-](https://doi.org/10.1175/1520-0450(1992)031<0708:NPINPI>2.0.CO;2)
1520 [0450\(1992\)031<0708:NPINPI>2.0.CO;2](https://doi.org/10.1175/1520-0450(1992)031<0708:NPINPI>2.0.CO;2), 1992.

1521 Mossop, S.C., Ruskin, R.E. and Heffernan, K.J.: Glaciation of a Cumulus at Approximately– 4C, *Journal of*
1522 *Atmospheric Sciences*, **25**(5), pp.889-899, [https://doi.org/10.1175/1520-](https://doi.org/10.1175/1520-0469(1968)025<0889:GOACAA>2.0.CO;2)
1523 [0469\(1968\)025<0889:GOACAA>2.0.CO;2](https://doi.org/10.1175/1520-0469(1968)025<0889:GOACAA>2.0.CO;2), 1968.

1524 Murray, B.J., O'sullivan, D., Atkinson, J.D. and Webb, M.E.: Ice nucleation by particles immersed in supercooled
1525 cloud droplets, *Chemical Society Reviews*, **41**(19), pp.6519-6554, doi:10.1039/c2cs35200a., 2012.

1526 Phillips, V.T., DeMott, P.J. and Andronache, C.: An empirical parameterization of heterogeneous ice nucleation for
1527 multiple chemical species of aerosol, *Journal of the Atmospheric Sciences*, **65**(9), pp.2757-2783,
1528 <https://doi.org/10.1175/2007JAS2546.1>, 2008.

1529 Plummer, D.M., McFarquhar, G.M., Rauber, R.M., Jewett, B.F. and Leon, D.C.: Structure and statistical analysis of
1530 the microphysical properties of generating cells in the comma head region of continental winter cyclones,
1531 *Journal of the Atmospheric Sciences*, **71**(11), pp.4181-4203, <https://doi.org/10.1175/JAS-D-14-0100.1>, 2014.

1532 Plummer, D. M., G. M. McFarquhar, R. M. Rauber, B. F. Jewett, and Leon., D. C.: Microphysical properties of
1533 convectively generated fall streaks in the comma head region of continental winter cyclones, *J. Atmos.*
1534 *Sci.*, **72**, 2465–2483, doi:10.1175/JAS-D-14-0354.1, 2015.

1535 Pruppacher, H. R., and Klett, J. D.: *Microphysics of Clouds and Precipitation*. 2d ed. Kluwer Academic, 954 pp.,
1536 1997.

- 1537 Ramelli, F., Henneberger, J., David, R.O., Bühl, J., Radenz, M., Seifert, P., Wieder, J., Lauber, A., Pasquier, J.T.,
1538 Engelmann, R. and Mignani, C.: Microphysical investigation of the seeder and feeder region of an Alpine
1539 mixed-phase cloud, *Atmospheric Chemistry and Physics*, 21(9), pp.6681-6706, [https://doi.org/10.5194/acp-](https://doi.org/10.5194/acp-21-6681-2021)
1540 [21-6681-2021](https://doi.org/10.5194/acp-21-6681-2021), 2021.
- 1541 [Rauber, R. M., Grant, L. O.: The characteristics and distribution of cloud water over the mountains of northern](#)
1542 [Colorado during winter-time storms. Part II: Spatial distribution and microphysical characteristics. J.](#)
1543 [Climate Appl. Meteor., 25, 489–504, https://doi.org/10.1175/1520-](#)
1544 [0450\(1986\)025<0489:TCADOC>2.0.CO;2, 1986.](#)
- 1545 Roach, W. T.: On the effect of radiative exchange on the growth by condensation of a cloud or fog droplet, *Quart. J.*
1546 *Roy. Meteor. Soc.*, 102, 361–372, <https://doi.org/10.1002/qj.49710243207>, 1976.
- 1547 Rogers, R.R. and Yau, M.K.: *A Short Course in Cloud Physics*. Pergamon Press, 294 pp., 1989.
- 1548 Rowe, P.M., Fergoda, M. and Neshyba, S.: Temperature-dependent optical properties of liquid water from 240 to 298
1549 K. *Journal of Geophysical Research: Atmospheres*, 125(17), <https://doi.org/10.1029/2020JD032624>, 2020.
- 1550 Roy, P., Rauber, R.M. and Girolamo, L.D.: A closer look at the evolution of supercooled cloud droplet temperature
1551 and lifetime in different environmental conditions with implications for ice nucleation in the evaporating
1552 regions of clouds, *Journal of the Atmospheric Sciences*. <https://doi.org/10.1175/JAS-D-22-0239.1>, 2023.
- 1553 Satoh, I., Fushinobu, K. and Hashimoto, Y.: Freezing of a water droplet due to evaporation—heat transfer dominating
1554 the evaporation–freezing phenomena and the effect of boiling on freezing characteristics, *International*
1555 *Journal of Refrigeration*, 25(2), pp.226-234, [http://dx.doi.org/10.1016/S0140-7007\(01\)00083-4](http://dx.doi.org/10.1016/S0140-7007(01)00083-4), 2002.
- 1556 Scardovelli, R. and Zaleski, S.: Direct numerical simulation of free-surface and interfacial flow, *Annual review of fluid*
1557 *mechanics*, 31(1), pp.567-603. <https://doi.org/10.1146/annurev.fluid.31.1.567>, 1999.
- 1558 Sedunov, Y. S.: *Physics of the Drop Formation in the Atmosphere*, John Wiley and Sons, 234 pp., 1974.
- 1559 Shaw, R.A., Durant, A.J. and Mi, Y.: Heterogeneous surface crystallization observed in undercooled water, *The*
1560 *Journal of Physical Chemistry B*, 109(20), pp.9865-9868, <https://doi.org/10.1021/jp0506336>, 2005.
- 1561 Srivastava, R.C. and Coen, J.L.: New explicit equations for the accurate calculation of the growth and evaporation of
1562 hydrometeors by the diffusion of water vapor, *Journal of Atmospheric Sciences*, 49(17), pp.1643-1651,
1563 [https://doi.org/10.1175/1520-0469\(1992\)049<1643:NEEFTA>2.0.CO;2](https://doi.org/10.1175/1520-0469(1992)049<1643:NEEFTA>2.0.CO;2), 1992.
- 1564 Standard Atmosphere: ISO 2533:1975, updated 2021: <https://www.iso.org/standard/7472.html>, 2021, last accessed
1565 09/26/2022.
- 1566 Szakáll, M., Debertshäuser, M., Lackner, C.P., Mayer, A., Eppers, O., Diehl, K., Theis, A., Mitra, S.K. and Borrmann,
1567 S.: Comparative study on immersion freezing utilizing single-droplet levitation methods, *Atmospheric*
1568 *Chemistry and Physics*, 21(5), pp.3289-3316, <https://doi.org/10.5194/acp-21-3289-2021>, 2021.
- 1569 Tabazadeh, A., Djikaev, Y.S., Hamill, P. and Reiss, H.: Laboratory evidence for surface nucleation of solid polar
1570 stratospheric cloud particles, *The Journal of Physical Chemistry A*, 106(43), pp.10238-10246,
1571 <https://doi.org/10.1021/jp021045k>, 2002a.
- 1572 Tabazadeh, A., Djikaev, Y.S. and Reiss, H.: Surface crystallization of supercooled water in clouds, *Proceedings of*
1573 *the National Academy of Sciences*, 99(25), pp.15873-15878, <https://doi.org/10.1073/pnas.252640699>, 2002b.

Formatted: Left

- 1574 Tessendorf, S.A., Boe, B., Geerts, B., Manton, M.J., Parkinson, S. and Rasmussen, R.: The future of winter orographic
 1575 cloud seeding: A view from scientists and stakeholders, *Bulletin of the American Meteorological Society*,
 1576 96(12), pp.2195-2198, <https://doi.org/10.1175/BAMS-D-15-00146.1>, 2015.
- 1577 [Tessendorf, S., Ikeda, K., Rasmussen, R., French, J., Rauber, R., Korolev, A., Xue, L., Blestrud, D., Dawson, N.,](#)
 1578 [Meadows, M., Kunkel, M. and Parkinson, S.: Characteristics of Generating Cells in Wintertime Orographic](#)
 1579 [Clouds. *Journal of the Atmospheric Sciences*, 81\(3\), pp. 649-673.](#)
 1580 <https://journals.ametsoc.org/view/journals/atsc/81/3/JAS-D-23-0029.1.xml>, 2024.
- 1581 Vaillancourt, P.A., Yau, M.K. and Grabowski, W.W.: Microscopic approach to cloud droplet growth by condensation.
 1582 Part I: Model description and results without turbulence, *Journal of the Atmospheric Sciences*, 58(14),
 1583 pp.1945-1964, [https://doi.org/10.1175/1520-0469\(2001\)058%3C1945:MATCDG%3E2.0.CO;2](https://doi.org/10.1175/1520-0469(2001)058%3C1945:MATCDG%3E2.0.CO;2), 2001.
- 1584 Vali, G.: Freezing Rate Due to Heterogeneous Nucleation. *J. Atmos. Sci.*, **51**, 1843–
 1585 1856, [https://doi.org/10.1175/1520-0469\(1994\)051<1843:FRDTHN>2.0.CO;2](https://doi.org/10.1175/1520-0469(1994)051<1843:FRDTHN>2.0.CO;2), 1994.
- 1586 Volmer, M.: *Kinetic der Phasenbildung* (Steinkopff, Dresden, Leipzig), 1939.
- 1587 Wang, Y., McFarquhar, G.M., Rauber, R.M., Zhao, C., Wu, W., Finlon, J.A., Stechman, D.M., Stith, J., Jensen, J.B.,
 1588 Schnaiter, M. and Järvinen, E.: Microphysical properties of generating cells over the Southern Ocean: Results
 1589 from SOCRATES, *Journal of Geophysical Research: Atmospheres*, 125(13),
 1590 <https://doi.org/10.1029/2019JD032237>, 2020.
- 1591 Watts, R.G.: Relaxation time and steady evaporation rate of freely falling raindrops, *Journal of Atmospheric Sciences*,
 1592 28(2), pp.219-225, [https://doi.org/10.1175/1520-0469\(1971\)028<0219:RTASER>2.0.CO;2](https://doi.org/10.1175/1520-0469(1971)028<0219:RTASER>2.0.CO;2), 1971.
- 1593 Watts, R.G. and Farhi, I.: Relaxation times for stationary evaporating liquid droplets, *Journal of the Atmospheric*
 1594 *Sciences*, 32(9), pp.1864-1867, [https://doi.org/10.1175/1520-](https://doi.org/10.1175/1520-0469(1975)032%3C1864:RTFSEL%3E2.0.CO;2)
 1595 [0469\(1975\)032%3C1864:RTFSEL%3E2.0.CO;2](https://doi.org/10.1175/1520-0469(1975)032%3C1864:RTFSEL%3E2.0.CO;2), 1975.
- 1596 Welti, A., Lüönd, F., Kanji, Z.A., Stetzer, O. and Lohmann, U.: Time dependence of immersion freezing: an
 1597 experimental study on size selected kaolinite particles. *Atmospheric Chemistry and Physics*, 12(20), pp.9893-
 1598 9907, 2012.
- 1599 Wexler, A.: Vapor pressure formulation for water in range 0 to 1008C. A revision, *J. Res. Natl. Bur. Stand. (U.S.)*,
 1600 80A, 775–785, <https://doi.org/10.6028%2Fjres.080A.071>, 1976.
- 1601 [White, F.M.: *Viscous Fluid Flow*, 3rd ed., McGraw-Hill, 2006, 656 pp.](#)
- 1602 Wright, T. P., and Petters, M.D.: The role of time in heterogeneous freezing nucleation, *J. Geophys. Res.*, 118, 3731–
 1603 3743, <https://doi.org/10.1002/jgrd.50365>, 2013.
- 1604 Yang, K., Hong, F. and Cheng, P.: A fully coupled numerical simulation of sessile droplet evaporation using Arbitrary
 1605 Lagrangian–Eulerian formulation. *International Journal of Heat and Mass Transfer*, 70, pp.409-420,
 1606 <https://doi.org/10.1016/j.ijheatmasstransfer.2013.11.017>, 2014.
- 1607 Young, K. C.: The Role of Contact Nucleation in Ice Phase Initiation in Clouds, *Journal of the Atmospheric Sciences*,
 1608 31, 768–776,
 1609 [https://doi.org/10.1175/1520-0469\(1974\)031<0768:TROCNI>2.0.CO;2](https://doi.org/10.1175/1520-0469(1974)031<0768:TROCNI>2.0.CO;2), 1974.

Formatted: Left

Formatted: Superscript

1610 Zaremba, T.J., Rauber, R.M., Heimes, K., Yorks, J.E., Finlon, J.A., Nicholls, S.D., Selmer, P., McMurdie, L.A. and
1611 McFarquhar, G.M.: Cloud-Top Phase Characterization of Extratropical Cyclones over the Northeast and
1612 Midwest United States: Results from IMPACTS, *Journal of the Atmospheric Sciences*, 81(2), pp.341-361,
1613 <https://doi.org/10.1175/JAMC-D-22-0154.1>, 2024.

1614
1615

Deleted: ¶

Page 10: [1] Formatted	Roy, Puja	5/10/24 8:51:00 PM
Font: 10 pt, Font color: Text 1		
Page 10: [1] Formatted	Roy, Puja	5/10/24 8:51:00 PM
Font: 10 pt, Font color: Text 1		
Page 10: [1] Formatted	Roy, Puja	5/10/24 8:51:00 PM
Font: 10 pt, Font color: Text 1		
Page 10: [2] Formatted	Roy, Puja	5/10/24 8:51:00 PM
Font: 10 pt, Font color: Text 1		
Page 10: [2] Formatted	Roy, Puja	5/10/24 8:51:00 PM
Font: 10 pt, Font color: Text 1		
Page 10: [3] Formatted	Roy, Puja	5/10/24 8:51:00 PM
Font: 10 pt, Font color: Text 1		
Page 10: [3] Formatted	Roy, Puja	5/10/24 8:51:00 PM
Font: 10 pt, Font color: Text 1		
Page 10: [3] Formatted	Roy, Puja	5/10/24 8:51:00 PM
Font: 10 pt, Font color: Text 1		
Page 10: [3] Formatted	Roy, Puja	5/10/24 8:51:00 PM
Font: 10 pt, Font color: Text 1		
Page 10: [3] Formatted	Roy, Puja	5/10/24 8:51:00 PM
Font: 10 pt, Font color: Text 1		
Page 10: [3] Formatted	Roy, Puja	5/10/24 8:51:00 PM
Font: 10 pt, Font color: Text 1		
Page 10: [3] Formatted	Roy, Puja	5/10/24 8:51:00 PM
Font: 10 pt, Font color: Text 1		
Page 10: [3] Formatted	Roy, Puja	5/10/24 8:51:00 PM
Font: 10 pt, Font color: Text 1		
Page 10: [3] Formatted	Roy, Puja	5/10/24 8:51:00 PM
Font: 10 pt, Font color: Text 1		
Page 10: [3] Formatted	Roy, Puja	5/10/24 8:51:00 PM
Font: 10 pt, Font color: Text 1		
Page 10: [4] Formatted	Roy, Puja	5/10/24 8:51:00 PM